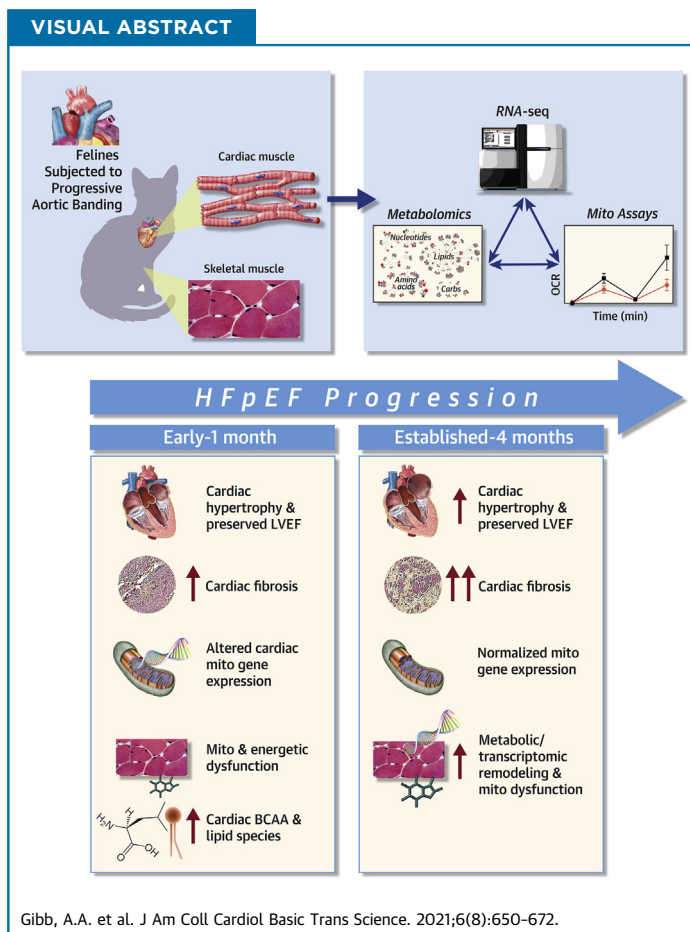**PRECLINICAL RESEARCH**

Molecular Signature of HFpEF

Systems Biology in a Cardiac-Centric Large Animal Model

Andrew A. Gibb, PhD,[a,*] Emma K. Murray, BS,[a,*] Deborah M. Eaton, BS,[b] Anh T. Huynh, BS,[a] Dhanendra Tomar, PhD,[a] Joanne F. Garbincius, PhD,[a] Devin W. Kolmetzky, BS,[a] Remus M. Berretta, BS,[b] Markus Wallner, MD, PhD,[b,c,d] Steven R. Houser, PhD,[b] John W. Elrod, PhD[a]

VISUAL ABSTRACT

Gibb, A.A. et al. J Am Coll Cardiol Basic Trans Science. 2021;6(8):650–672.

HIGHLIGHTS

- Early cardiac mitochondrial dysfunction is mediated by transcriptional down-regulation of the mitochondrial proteome.
- Comprehensive metabolic remodeling is conserved throughout HFpEF progression and includes increased amino acid and lipid species, indicative of impaired oxidative metabolism.
- Transcriptional and metabolic remodeling of skeletal muscle suggests cardiac signaling as a mediator of peripheral tissue maladaptation.
- Unbiased systems-level analysis provides new mechanisms underlying HFpEF development.

From the [a]Center for Translational Medicine, Lewis Katz School of Medicine at Temple University, Philadelphia, Pennsylvania, USA; [b]Cardiovascular Research Center, Lewis Katz School of Medicine at Temple University, Philadelphia, Pennsylvania, USA; [c]Division of Cardiology, Medical University of Graz, Graz, Austria; and the [d]Center for Biomarker Research in Medicine, CBmed GmbH, Graz, Austria.
*Dr Gibb and Ms Murray contributed equally to this work.

The authors attest they are in compliance with human studies committees and animal welfare regulations of the authors' institutions and Food and Drug Administration guidelines, including patient consent where appropriate. For more information, visit the Author Center.

SUMMARY

In this study the authors used systems biology to define progressive changes in metabolism and transcription in a large animal model of heart failure with preserved ejection fraction (HFpEF). Transcriptomic analysis of cardiac tissue, 1-month post-banding, revealed loss of electron transport chain components, and this was supported by changes in metabolism and mitochondrial function, altogether signifying alterations in oxidative metabolism. Established HFpEF, 4 months post-banding, resulted in changes in intermediary metabolism with normalized mitochondrial function. Mitochondrial dysfunction and energetic deficiencies were noted in skeletal muscle at early and late phases of disease, suggesting cardiac-derived signaling contributes to peripheral tissue maladaptation in HFpEF. Collectively, these results provide insights into the cellular biology underlying HFpEF progression. (J Am Coll Cardiol Basic Trans Science 2021;6:650–672) © 2021 The Authors. Published by Elsevier on behalf of the American College of Cardiology Foundation. This is an open access article under the CC BY-NC-ND license (http://creativecommons.org/licenses/by-nc-nd/4.0/).

**ABBREVIATIONS
AND ACRONYMS**

BCAA = branched chain amino acids

DAG = diacylglycerol

ECM = extracellular matrix

EF = ejection fraction

ESI = electrospray ionization

ETC = electron transport chain

FC = fold change

FDR = false discovery rate

GO = gene ontology

HF = heart failure

HFpEF = heart failure with preserved ejection fraction

HFrEF = heart failure with reduced ejection fraction

LA = left atrial

LAV = left atrial volume

LV = left ventricle/ventricular

m/z = mass to charge ratio

MS/MS = tandem mass spectrometry

RCR = respiratory control ratio

RI = retention index

UPLC = ultraperformance liquid chromatography

Cardiovascular disease is the leading cause of death worldwide, with nearly 20% of all-cause mortality being cardiac related. Several etiologies result in heart failure (HF), including coronary artery disease, hypertension, and myocarditis (1,2). Additionally, other chronic diseases, such as diabetes and obesity, contribute to the development of heart failure (3). In the United States alone, HF affects approximately 6 million individuals a year with a financial burden of nearly $31 billion (4,5). HF is divided into 3 general clinical categories based on cardiac function: HF with reduced ejection fraction (HFrEF) (EF <40%), HF with mid-range ejection fraction (EF) (41%-49%), and HF with preserved ejection fraction (HFpEF) (EF >50%) (6). Of these, HFpEF accounts for ~50% of all HF cases with a growing incidence rate of 10% per decade (6). Despite the prevalence of HFpEF, our understanding of the pathophysiological mechanisms contributing to HFrEF is substantially greater due to the fact that animal models of HFrEF more adequately recapitulate the human condition (7). For example, murine studies of neurohormonal imbalance in HF led to clinical trials proving the efficacy of neurohormonal pathway inhibitors in improving patient outcomes and reducing mortality (7). Unfortunately, efficacy of these drugs was not found in HFpEF patients, likely indicating distinct pathological mechanisms of disease (7-13).

A major challenge in studying HFpEF in preclinical models is the ability to recapitulate the clinical features of human HFpEF which include exertional dyspnea, fatigue, pulmonary hypertension, left ventricular (LV) diastolic dysfunction, and exercise intolerance (14). Although rodent HFpEF models have allowed for greater understanding of the mechanisms contributing to LV diastolic dysfunction, their small size and differences in physiological properties compared with large mammals present significant limitations to recapitulating features of HFpEF (15). Further, the numerous comorbidities associated with HFpEF present numerous model and experimental design complications. The Houser lab recently established a feline model of HFpEF's multi-factorial clinical features, including LV hypertrophy, elevated LV filling pressures (LV end-diastolic pressure), left atrial (LA) enlargement, and impaired pulmonary mechanics contri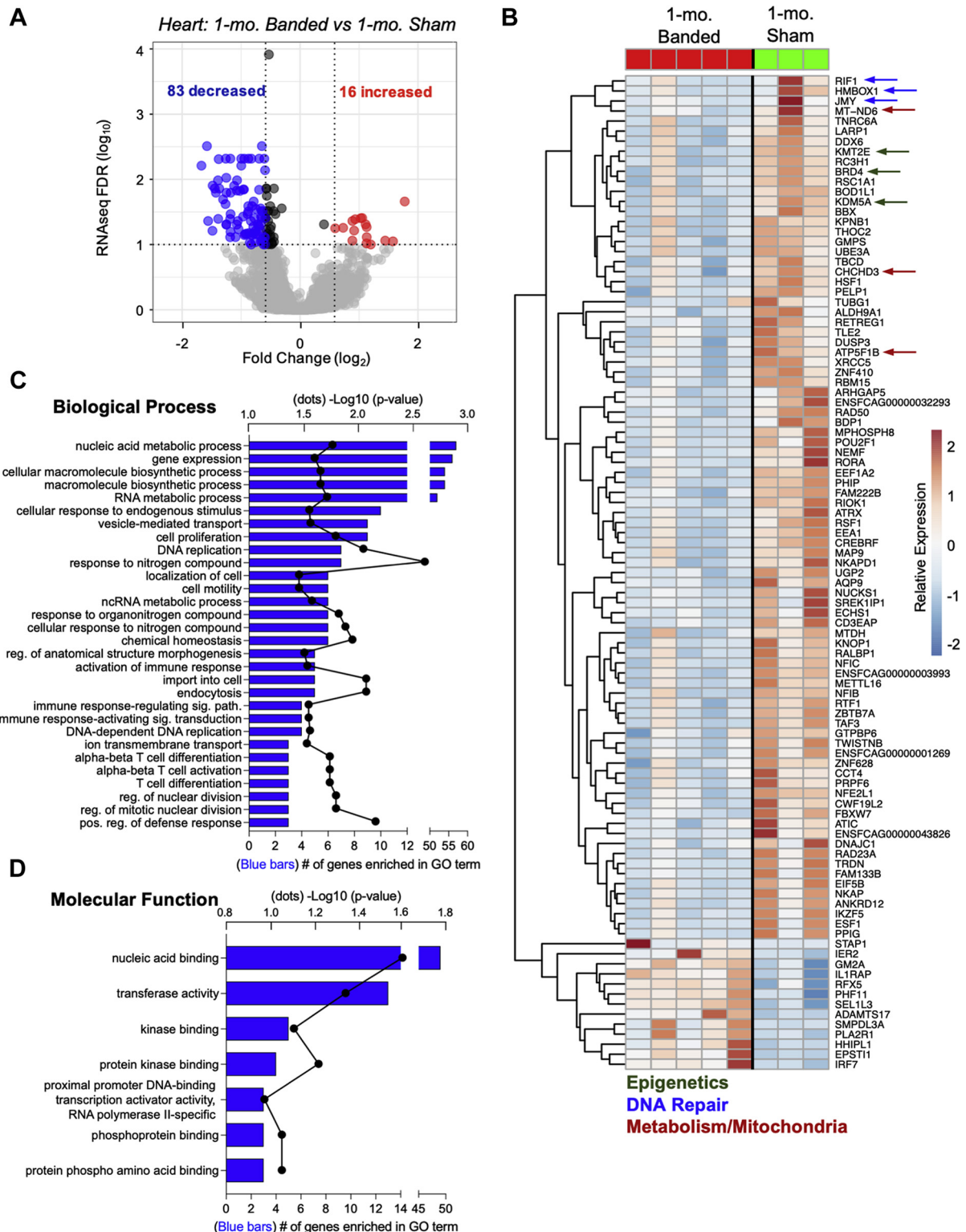buting to functional compromise and poor oxygenation (16). Furthermore, the model was amendable to therapeutic intervention as it was reported that treatment with SAHA (suberoylanilide hydroxamic acid, also known as vorinostat), a pan histone-deacetylase (HDAC) inhibitor, was sufficient to prevent, and possibly reverse, disease indices (17). Another benefit of this model is that it lacks comorbidities such as age, obesity, and diabetes, allowing for mechanistic study of the cardiac contributions to HFpEF.

Derangements in myocardial metabolism are a key feature of the pathological heart. Global unbiased metabolomic screens previously performed in various models of HFrEF have revealed a shift from oxidative to glycolytic metabolism and alterations in various amino acids, providing mechanistic insight into cardiac pathophysiology (18,19). RNA sequencing has also allowed for the unbiased examination of transcriptomic changes during HF, which have identified significant alterations to genes associated with mitochondria, oxidative phosphorylation, cardiac hypertrophy, and cell death (20). Importantly, integration of these 2 omics approaches revealed that the metabolic derangements occurring early in HFrEF involve both transcriptional and post-transcriptional events (18); however, these approaches have yet to be used

FIGURE 1 1-Month Aortic Banding Reveals a Cardiac RNAseq Signature of Transcriptional and Post-Transcriptional Regulation, Mitochondrial Dysfunction, and Inflammation

in HFpEF due to the lack of a reliable model. Here, we interrogated the early cardiac and skeletal muscle transcriptional and metabolic signatures in a feline banding model to aid our understanding of HFpEF pathogenesis and identify primary mechanisms driving disease progression and potential therapeutic targets.

METHODS

ANIMAL PROCEDURES. All animal procedures were approved by the Temple University School of Medicine Institutional Animal Care and Use Committee. We used a total of 18 male shorthair kittens (aged 2 months [1.3 kg]) (Liberty Research Inc), that underwent either aortic constriction (n = 10, with customized preshaped bands or a sham procedure (n = 8). Before surgery, baseline phenotyping was performed, and animals were randomly assigned to their respective groups. Animals were sedated with ketamine (25 mg/kg) and acepromazine (0.1 mg/kg), intubated, and mechanically ventilated (Narkomed 2b, Dräger). Surgical (plane) anesthesia was maintained throughout the procedure with 1%-2% isoflurane mixed with 100% oxygen. Under sterile conditions, a 2- to 4-cm skin incision was made over the 3rd and 4th intercostal space and extended through the intercostal muscles. The pericardium was opened, and the aorta was dissected from the pulmonary artery. The preshaped band was placed around the ascending aorta and gently tied down without causing significant constriction of the aorta. Animals received heat support during anesthesia and recovery. In contrast to immediate pressure overload, this approach results in a slow progressive pressure overload during growth, as the cats grow into the aortic band. Cats were group housed in spacious rooms that were enriched with scratching posts, climbing towers, and a hammock where they could freely move and were provided with food and water ad libitum. No animals were excluded from study.

TRANSTHORACIC ECHOCARDIOGRAPHY. Echo was performed with a Vivid q Vet Premium BT12 (GE Healthcare) using a 12S-RS sector probe at baseline and 1 month post-surgery, and 4 months post-surgery, as previously described (16,17). Animals

were sedated with an intramuscular injection of alfaxalone (1 mg/kg), butorphanol (0.5 mg/kg), and midazolam (0.5 mg/kg). Alfaxalone is a neuroactive steroid molecule with properties of a general anesthetic. Alfaxalone does not cause an increase in heart rate, which is occasionally observed with ketamine. Ivabradine (0.3 mg/kg) was administered intravenously before echo to decrease the heart rate to around 150 beats/min to ensure reliable diastolic assessment (21). Echocardiographic measurements were subsequently performed offline in a blinded fashion with EchoPAC SW v201 plugin (GE Healthcare). Anterior and posterior wall thickness was measured at end-diastole from the parasternal short-axis view at the level of the papillary muscle. The average of the anterior and posterior wall was reported. The LA aortic root ratio (LA/Ao) was measured in early ventricular diastole using the first frame after aortic ejection using the right parasternal short-axis view (22). LA volume (LAV) and LA area were calculated as described in humans (23) from a right parasternal long-axis view, using the Simpson's rule at end-systole and end-diastole. LA function, assessed by LA volumes, was calculated according to atrial function studies in humans (24). Changes in LAV expressed as ejection fraction (LA-EF = [LAVmax − LAVmin]/LAVmax) (25). LV end-diastolic diameter and fractional shortening were measured in b-mode from a right parasternal short-axis view. Echocardiographic results for the 4-month time point can be found here (16). Tissues from this previous published cohort were used in the current transcriptomic and metabolomic experiments.

HEART TISSUE COLLECTION AND PROCESSING. Hearts were removed, rinsed, and weighed. The aorta was cannulated, and the coronary arteries were cleared by perfusion with cold Krebs-Henseleit buffer. Before tissue fixation, small pieces of the anterior-lateral LV were collected and immediately flash frozen for transcriptomic and metabolomic profiling. For mitochondrial assays, fresh tissue was used immediately following isolation. The hearts were then gravity perfused with 10% formalin at mean arterial pressure (100 mm Hg). Fixed hearts were immersed overnight in 10% formalin and then

---

FIGURE 1 Continued

Differential expression and gene enrichment analysis in hearts subjected to RNAseq 1-month post-banding were compared with sham controls. **(A)** Volcano plot of differentially expressed RNA transcripts indicating the number of genes increased and decreased in expression (fold change ≥1.5; FDR ≤ 0.1); **(B)** heatmap of the 99 genes found to be differentially expressed. Gene ontology (GO) analysis revealing the **(C)** biological processes and **(D)** molecular functions of those genes found to be differentially expressed. n = 3 sham and 5 banded. FDR = false discovery rate.

FIGURE 2   Cardio-Metabolic Remodeling Is a Characteristic Feature of Early HFpEF Development
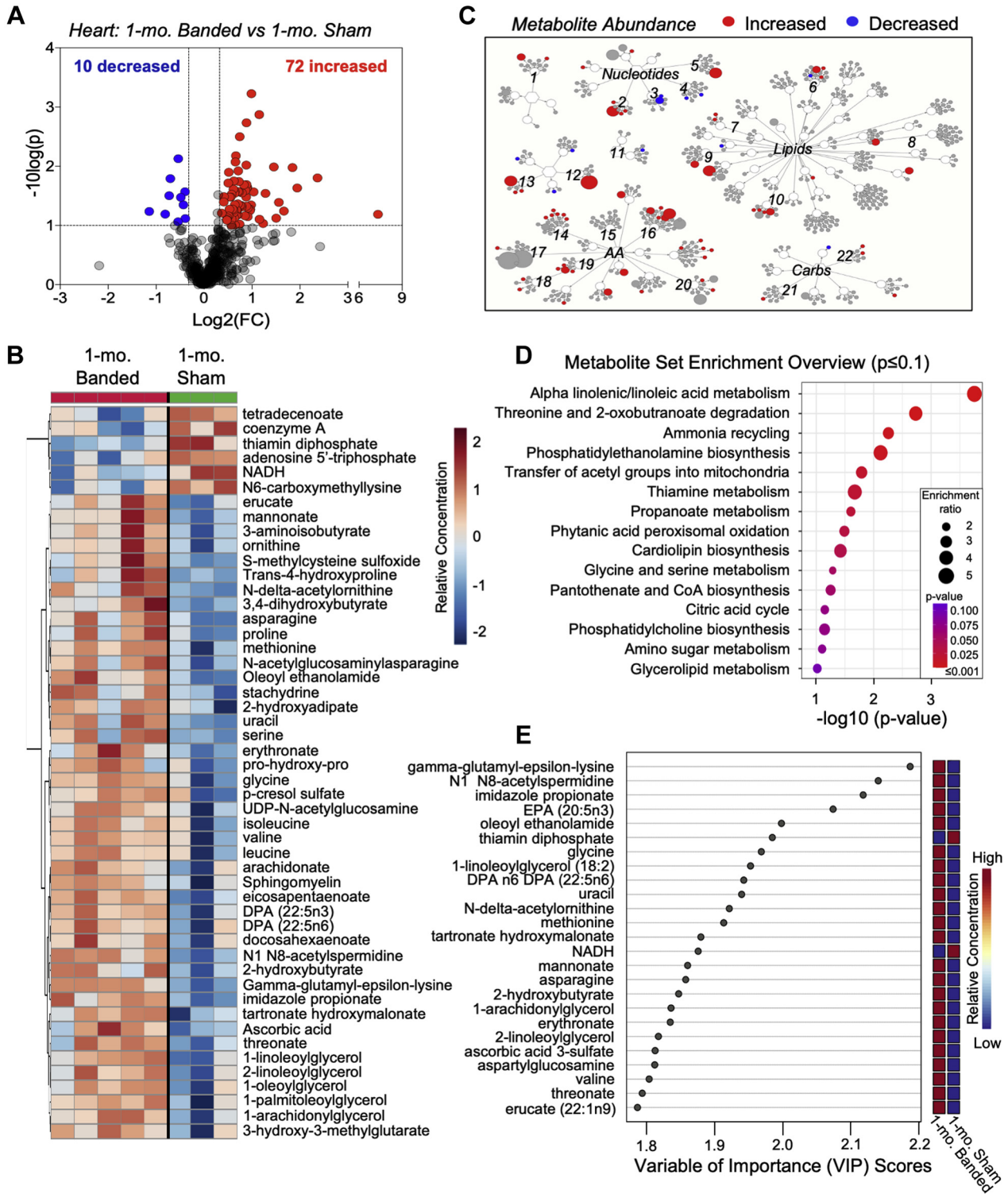
stored in 70% ethanol for up to 1 week before being processed. The heart was cut on a short-axis plane, starting at the apex and continuing up to the base, and then short-axis sections were cut in half (lateral and septal wall) and embedded in paraffin wax blocks. Tissue sections (5-μm) from 2 different levels from each sample were slide-mounted (AML Laboratories).

HEART HISTOLOGY. Paraffin-embedded LV samples fixed at 1 month post-banding were stained with Masson's Trichrome (Sigma-Aldrich) to determine percentage of fibrosis. Cytoplasm and muscle fibers stain red, whereas collagen (fibrosis) stains blue. The stained slides were imaged at 10× magnification (Nikon Eclipse Ni, NIS Elements software), stitched into 2 × 2 larger images, and analyzed using ImageJ software (National Institutes of Health) with color threshold analysis. The percentage of fibrotic tissue was determined as the collagen-positive tissue of the total stained LV tissue. In order to examine the LV fibrosis gradient, the subendocardium and subepicardium were imaged and quantified separately. All analyses were performed in a blinded fashion. Previously reported fibrosis quantifications for the 4-month time point were used for correlations with metabolomics data in the current study (16).

RNA SEQUENCING. Anterior-lateral LV, immediately flash frozen in liquid nitrogen following excision to most accurately capture the cardiac transcriptome as it is in vivo, was subjected to RNAseq analysis. Skeletal muscle isolated from the gastrocnemius was also immediately flash frozen in liquid nitrogen. Total RNA was isolated using a fibrous tissue RNA isolation kit (Qiagen). The TrueSeq stranded mRNA library prep kit was used to enrich polyA mRNAs via poly-T-based RNA purification beads, which were then amplified using HiSeq rapid SR cluster kit, and then multiplexed and run using the HiSeq rapid SBS kit. Reading depth was ∼30 M reads per sample, and single-end 75-bp fragments were generated for bioinformatic analysis. All kits for sequencing were obtained from Illumina, and all

sequencing was performed on the Illumina HiSeq2500 sequencer. RNA transcripts were aligned to the *felis_catus*_9.0 assembly using HISAT2 v2.1.0 and quantified using HTSeq v0.11.2. Differential expression analysis was performed between banded and sham samples using DESeq2 v1.22.2. Genes were considered significantly differentially expressed when they met a fold change ≥1.5 and a false discovery rate (FDR) ≤0.1. Data were visualized using R v3.5.3 (R Foundation for Statistical Computing) packages pHeatmap v1.0.12 and clusterProfiler v3.10.1. Gene ontology (GO) analysis was accomplished using orthologous human (*homo sapiens* ensemble 38) annotations obtained via BioMart v2.38.0 and ClusterProfiler GO analysis tools. All RNA-sequencing data has been submitted to the GEO (Gene Expression Omnibus) repository with the accession #GSE181184.

METABOLOMIC ANALYSIS. Anterior LV tissue was immediately flash frozen in liquid nitrogen following excision to most accurately capture the cardiac metabolome as it is in vivo, and subjected to unbiased metabolomics. Skeletal muscle isolated from the gastrocnemius was likewise flash frozen in liquid nitrogen. Samples were prepared by Metabolon using their automated MicroLab STAR system (Hamilton Company). First, tissue homogenates were made in water at a ratio of 5 μL per mg of tissue. For quality control, several recovery standards were added before the first step in the extraction process. To remove protein, small molecules bound to protein or trapped in the precipitated protein matrix were dissociated, and to recover chemically diverse metabolites, proteins were then precipitated with methanol (final concentration 80% v/v) under vigorous shaking for 2 minutes (Glen Mills GenoGrinder 2000) followed by centrifugation. For quality assurance and control, a pooled matrix sample was generated by taking a small volume of each experimental sample to serve as a technical replicate throughout the data set. Extracted water samples

FIGURE 2   Continued

Metabolic phenotyping of hearts subjected to 1-month aortic banding compared with sham controls: **(A)** Volcano plot analysis showing metabolites with a fold change (FC) ≥1.25-fold; $P \leq 0.1$; **(B)** heatmap of the top 50 significantly different metabolites; **(C)** metabolic network visualization of metabolites in 1-month banded hearts as compared with sham control hearts. **Colored circles** indicate a statistically significant difference with the size of the circle indicative of the degree of change: 1. gamma-glutamyl amino acids; 2. inosine purines; 3. cytidine pyrimidines; 4. adenine purines; 5. uracil pyrimidines; 6. long-chain polyunsaturated fatty acids; 7. poly-, un-, saturated fatty acid species; 8. phospholipids; 9. mono- and dicarboxylic fatty acids; 10. monoacylglycerols; 11. TCA cycle; 12. vitamin B6 metabolism; 13. ascorbate metabolism; 14. Met, Cys, SAM metabolism; 15. lysine metabolism; 16. Leu, Ile, Val metabolism; 17. His metabolism; 18. Ala, Asp metabolism; 19. Gly, Ser, Thr metabolism; 20. Trp metabolism; 21. glycolytic intermediates; 22. amino sugars; **(D)** enrichment overview of the metabolic pathways significantly affected. Only pathways with a $P \leq 0.1$ shown; **(E)** partial least squares-discriminant analysis variables of importance projection indicative of the metabolites most responsible for group separation. n = 3 sham and 5 banded. AA = amino acids; Carbs = carbohydrates; HFpEF = heart failure with preserved ejection fraction.

FIGURE 3   Correlations Between the Cardio-Metabolic Profile and Mitochondrial Function Highlight an Energetic and Functional Decline During Early Cardiac Remodeling
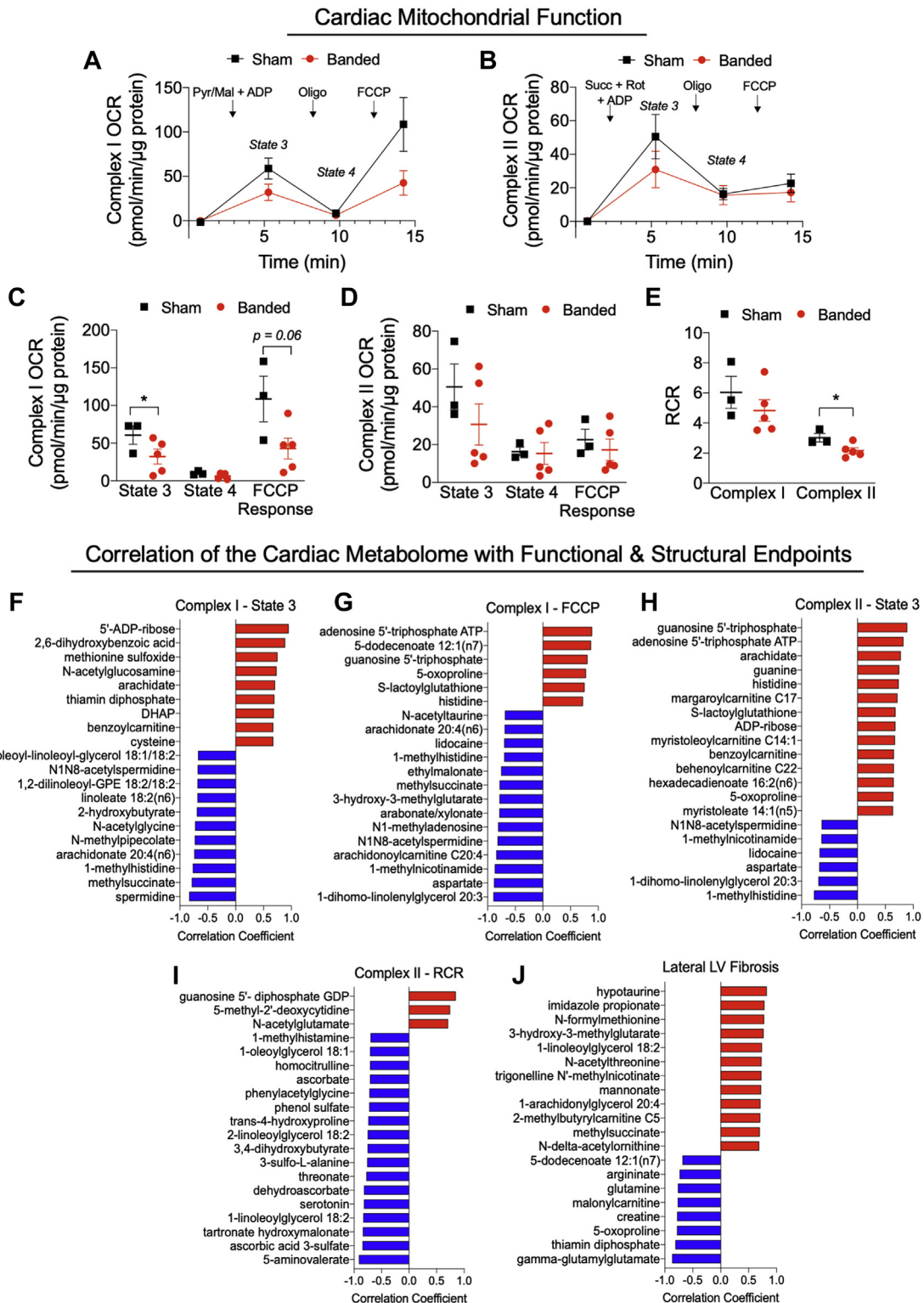
served as process blanks. A cocktail of standards known not to interfere with the measurement of endogenous compounds was spiked into every analyzed sample, allowing instrument performance monitoring and aiding chromatographic alignment.

The extract was divided into fractions for analysis by reverse phase ultraperformance liquid chromatography (UPLC)-tandem mass spectrometry (UPLC-MS/MS) with positive ion mode electrospray ionization (ESI), by reverse phase UPLC-MS/MS with negative ion mode ESI, and by hydrophilic interaction UPLC-MS/MS with negative ion mode ESI. Samples were placed briefly on a TurboVap (Zymark) to remove the organic solvent. All methods used a Waters ACQUITY UPLC and a Thermo Scientific Q-Exactive high resolution/accurate mass spectrometer interfaced with a heated electrospray ionization (HESI-II) source and Orbitrap mass analyzer operated at 35,000 mass resolution. The sample extract was reconstituted in solvents compatible with each MS/MS method. Each reconstitution solvent contained a series of standards at fixed concentrations to ensure injection and chromatographic consistency. One aliquot was analyzed using acidic positive ion conditions, chromatographically optimized for hydrophilic compounds. In this method, the extract was gradient eluted from a C18 column (Waters UPLC BEH C18-2.1 $\times$ 100 mm, 1.7 μm) using water and methanol, containing 0.05% perfluoropentanoic acid and 0.1% formic acid. For more hydrophobic compounds, the extract was gradient eluted from the aforementioned C18 column using methanol, acetonitrile, water, 0.05% perfluoropentanoic acid, and 0.01% formic acid. Aliquots analyzed using basic negative ion optimized conditions were gradient eluted from a separate column using methanol and water, containing 6.5 mmol/L ammonium bicarbonate (pH 8). The last aliquot was analyzed via negative ionization following elution from a hydrophilic interaction column (Waters UPLC BEH Amide 2.1 $\times$ 150 mm, 1.7 μm) using a gradient consisting of water and acetonitrile with 10 mmol/L ammonium formate (pH 10.8). The MS analysis alternated between MS and data-dependent MS^n scans using dynamic exclusion. The scan range covered 70-1000 mass to charge ratios (m/z).

Raw data were extracted, peak-identified, and processed using Metabolon's proprietary hardware and software. Compounds were identified by comparison to library entries of purified, authenticated standards or recurrent unknown entities, with known retention times/indices (RI), m/z, and chromatographic signatures (including MS/MS spectral data). Biochemical identifications were based on 3 criteria: RI within a narrow RI window of the proposed identification, accurate mass match to the library ± 10 ppm, and the MS/MS forward and reverse scores between experimental data and authentic standards. Proprietary visualization and interpretation software (Metabolon) was used to confirm the consistency of peak identification among the various samples. Library matches for each compound were checked for each sample and corrected, if necessary. Area under the curve was used for peak quantification.

Original scale data (raw area counts) were analyzed using MetaboAnalyst 4.0 software. Metabolites with >50% of the values missing were omitted from the analysis, and missing values were imputed by introducing values with one-fifth of the minimum positive value of each variable. An interquartile range filter was used to identify and remove variables unlikely to be of use when modeling the data. The data were log-transformed (base log-10) and standardized (mean-centered and divided by the standard deviation of each variable). Univariate (eg, volcano plots) and multivariate (eg, principal component analysis) analyses were then performed. Unadjusted P values (p ≤ 0.1) were used to determine significance. Fold changes and P values for all metabolites found to be significantly different are listed in Supplemental Tables 1-8. The raw metabolomics data from individual cats were used for correlative comparison (pairwise analysis; Pearson's correlations) with mitochondrial functional and tissue fibrosis.

MITOCHONDRIAL FUNCTION. Heart and skeletal muscle mitochondria were isolated from fresh tissue and subjected to respiratory function assays using the Seahorse XF96 (Agilent), as described previously ([17],[26]). Briefly, ~100 mg of anterior-lateral LV was washed 5$\times$ with cold buffer A (220 mmol/L mannitol, 70 mmol/L sucrose, 5 mmol/L MOPS, 1 mmol/L EDTA;

FIGURE 3 Continued

(A and B) Interrogation of mitochondrial function following 1-month of aortic banding: state 3 (substrate-mediated), state 4 (oligomycin inhibition of complex V), and FCCP-mediated (maximal respiratory capacity) oxygen consumption rates (OCRs) in isolated cardiac mitochondria. Quantification of state 3, state 4, and FCCP-mediated rates for **(C)** complex I (pyruvate + malate)-specific substrates and **(D)** complex II (succinate)-specific substrates + rotenone (complex I inhibitor); **(E)** quantification of respiratory control ratios (state 3/state 4), providing an index of oxygen consumption to ATP-production coupling; Metabolite correlations with **(F)** complex I – state 3 and **(G)** FCCP mediated rates; metabolite correlations with **(H)** complex II–state 3 and **(I)** respiratory control ratio (RCR). Metabolite correlations with **(J)** cardiac fibrosis. The raw metabolomic data from each individual cat were used to make the correlations to the functional parameters indicated in each graph. All correlations have a $P \leq 0.1$. n = 3 sham and 5 banded. *$P \leq 0.05$. LV = left ventricular.

FIGURE 4   Changes in Metabolism, Cell Signaling, and Inflammation Define the Cardiac Transcriptomic Signature Following the Progression to HFpEF
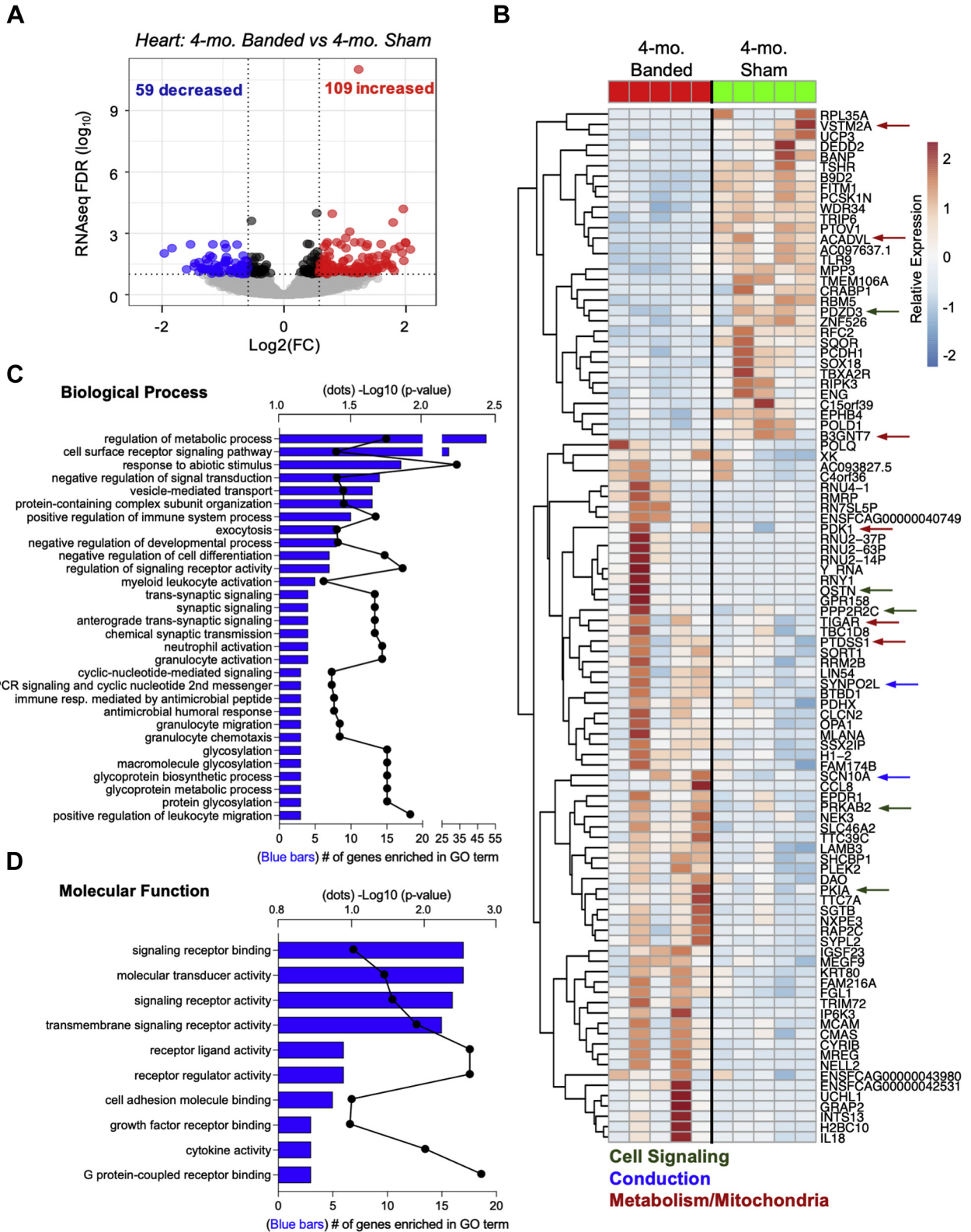
pH 7.2 with potassium hydroxide) followed by homogenization using a glass-col homogenizer in 2 ml of buffer A containing 0.2% fatty acid-free bovine serum albumin. Homogenate was then subjected to centrifugation at 800g for 10 minutes followed by supernatant collection and centrifugation at 10,000g for 10 minutes. The pellet containing mitochondria was then resuspended in 1 ml of fresh buffer A (without bovine serum albumin) and centrifuged at 10,000g, with this step repeated once. The washed mitochondrial pellet was then resuspended in 150 μL of respiration buffer (120 mmol/L KCl, 25 mmol/L sucrose, 10 mmol/L HEPES, 1 mmol/L MgCl$_2$, 5 mmol/L KH$_2$PO$_4$; pH 7.2 with potassium hydroxide) and kept on ice.

To determine mitochondrial function, samples were diluted to a concentration of 5 μg (protein) in 50 μL of respiration buffer per well and centrifuged onto XF96 microplates at 500g for 3 minutes at 4 °C. State 3 respiration in response to substrates was measured after injection of pyruvate + malate (5.0 mmol/L + 2.5 mmol/L, final concentrations) or succinate + rotenone (10 mmol/L + 1 μmol/L, final concentrations) to assess complex I and II rates, respectively. Fatty acid oxidation rates were assessed by injection of palmitoyl-L-carnitine (50 μmol/L). The oxygen consumption rates recorded after injection of oligomycin (1 μg/mL), an inhibitor of ATP synthase, served as a measure of state 4 respiration. Following state 4 respiratory measurements, injection of FCCP, a mitochondrial uncoupler, provided electron transport chain (ETC) complex maximal respiratory capacity. Respiratory control ratios, state 3/state 4, were calculated as a measure of the coupling of oxygen consumption to ATP production.

STATISTICAL ANALYSIS. Statistical analysis was performed using GraphPad Prism 9 (GraphPad Software), MetaboAnalyst, and R version 3.6. Statistical parameters including the value of n (number of cats), the definition of center, precision (mean), and dispersion (SEM or SD) measures are reported. A P value of ≤0.05 was considered statistically significant. For the metabolomics data set, an unadjusted P value of ≤0.1 was considered statistically significant. For the transcriptomics data set, a FDR of ≤0.1 was

considered statistically significant. For direct comparisons, statistical significance was calculated by unpaired or paired Student's t-test for between or within group comparisons, respectively. Details on the statistical methods employed for the metabolomics and RNA-sequencing (RNA-seq) data sets can be found within their respective methods sections.

RESULTS

ONE-MONTH AORTIC BANDING REVEALS IMPAIRMENTS IN TRANSCRIPTIONAL AND POST-TRANSCRIPTIONAL REGULATION, MITOCHONDRIAL DYSFUNCTION, AND INFLAMMATION. Following 1-month aortic banding, LV function was largely unchanged with no significant difference in LV end-diastolic, end-systolic diameter, or fractional shortening (Supplemental Figures 1A to 1F). Modest LA remodeling was observed, with a small, but significant, increase in LA end-systolic volume. No differences in LA EF or LA systolic diameter, as a ratio to the aortic root (LA/Ao; a measure of atrial dilation), were observed (Supplemental Figures 1G to 1L). Significant cardiac hypertrophy 1 month post-banding indicated by echocardiographic measurements of end-diastolic LV wall thickness and increased heart weight to body weight ratio were observed (Supplemental Figures 1M to 1O). Tissue fibrosis, a common feature of HFpEF cardiac pathophysiology, which, we previously reported, is present 4 months post-aortic banding (16,17), was noted 1 month post-banding (Supplemental Figures 1P to 1R), suggesting fibrotic initiation precedes the development of HFpEF-related functional decline. Collectively, echocardiographic results confirm early cardiac remodeling in the form of LV hypertrophy and interstitial fibrosis in the absence of systolic or diastolic functional decline.

To identify potential molecular pathways and targets contributing early in HFpEF-like disease, we isolated RNA from the LV and performed next-gen RNA-seq. We observed changes in the expression of 99 genes post-banding, with 83 of these down-regulated (fold change [FC] ≥1.5 and FDR ≤0.1) (**Figures 1A and 1B**). GO analysis of differentially expressed genes identified processes associated with transcriptional regulation (eg, gene expression,

---

FIGURE 4 Continued

Metabolomic and RNAseq analyses of hearts 4 months post-banding compared with age-matched shams. **(A)** Volcano plot of differentially expressed RNA transcripts indicating the number of genes increased and decreased in expression (fold change [FC] ≥1.5; *FDR* ≤ 0.1); **(B)** heatmap of the top 100 genes found to be differentially expressed. Gene ontology (GO) analysis revealing the **(C)** biological processes and **(D)** molecular functions of those genes found to be differentially expressed. n = 5 sham and 5 banded. FDR = false discovery rate; HFpEF = heart failure with preserved ejection fraction.

FIGURE 5   Metabolic Analysis of the Heart 4 Months Post-Banding Reveals a Sustained Remodeling of Amino Acid Metabolism and a Greater Reliance on Aerobic Glycolysis for Energy Provision
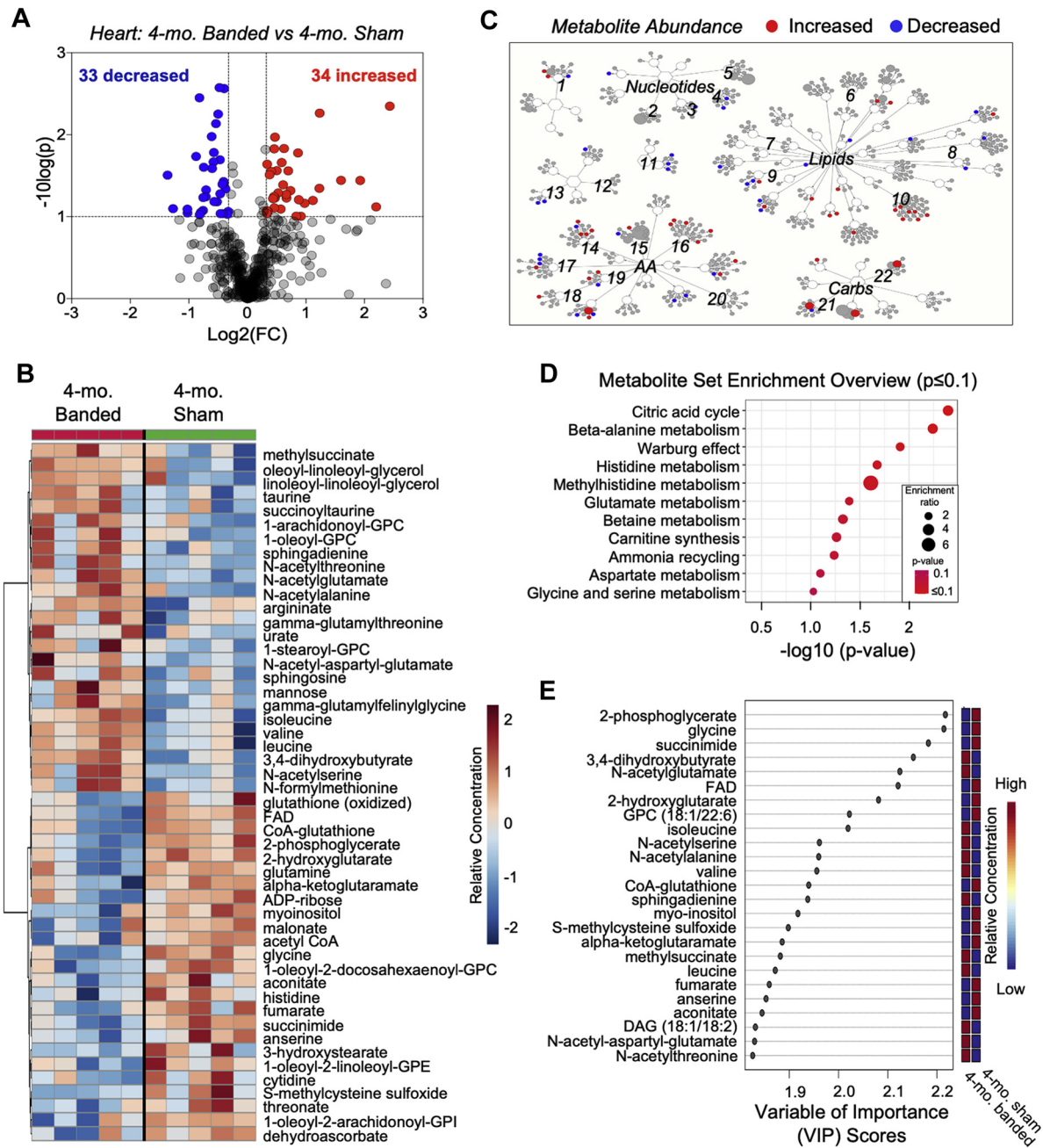
Metabolic phenotyping of hearts 4 months post-aortic banding compared with age-matched shams: **(A)** Volcano plot analysis showing metabolites with a fold change (FC) ≥1.25-fold; $P \leq 0.1$; **(B)** heatmap of the top 50 significantly different metabolites; **(C)** metabolic network visualization of metabolites in 4-month banded hearts as compared with sham control hearts. **Colored circles** indicate a statistically significant difference with the size of the circle indicative of the degree of change: 1. gamma-glutamyl amino acids; 2. inosine purines; 3. cytidine pyrimidines; 4. adenine purines; 5. uracil pyrimidines; 6. long-chain polyunsaturated fatty acids; 7. poly-, un-, saturated fatty acid species; 8. phospholipids; 9. mono- and dicarboxylic fatty acids; 10. monoacylglycerols; 11. TCA cycle; 12. vitamin B6 metabolism; 13. ascorbate metabolism; 14. Met, Cys, SAM metabolism; 15. lysine metabolism; 16. Leu, Ile, Val metabolism; 17. His metabolism; 18. Ala, Asp metabolism; 19. Gly, Ser, Thr metabolism; 20. Trp metabolism; 21. glycolytic intermediates; 22. amino sugars; **(D)** enrichment overview of the metabolic pathways significantly affected. Only pathways with a $P \leq 0.1$ shown; **(E)** partial least squares-discriminant analysis variables of importance projection indicative of the metabolites most responsible for group separation. n = 5 sham and 5 banded. AA = amino acids; Carbs = carbohydrates.

nucleic acid and RNA metabolic processes) among the top enriched pathways (**Figure 1C**). Several epigenetic modifiers were found to be down-regulated in the banded heart (eg, *BRD4*, *KMT2E*, *KDM5A*), suggesting chromatin reorganization early in disease. Molecular function enrichment identified nucleic acid binding proximal promoter DNA-binding transcription activator activity, as well as RNA polymerase II regulation, as system-wide alterations 1 month post-banding (**Figure 1D**). Several genes involved in the DNA repair pathway (eg, *RIF1*, *MHBOX2*, *JMY*) were down-regulated (**Figure 1C**), which may underlie the HFpEF hypertrophic phenotype (27).

Several biosynthetic metabolic processes (eg, macromolecule, nucleic acid, and RNA metabolic processes) were highly enriched (**Figure 1C**); however, interestingly, few genes directly related to metabolism were differentially expressed. We did observe a significant decrease in genes associated with the mitochondrial ETC, such as *MT-ND6* and *ATP5F1B*, which are critical core subunits of complex I and ATP synthase (**Figure 1B**). Furthermore, *CHCHD3*, an inner mitochondrial membrane scaffold protein required for mitochondrial cristae structural integrity, was down-regulated, which is reported to impair oxygen consumption and ATP production (28) (**Figure 1B**). Although intermediary metabolic pathways did not differ at the transcriptional level, several GO terms associated with enzymatic function/activity, including protein kinase and phosphoprotein binding, were significantly enriched (**Figure 1D**), possibly suggesting alterations in the post-translational regulation of cellular metabolism. Immune response pathways were also identified (eg, T-cell differentiation, activation of immune response) (**Figure 1C**), suggesting inflammatory signaling may be an early driver of HFpEF progression. Indeed, systemic inflammation brought upon by the numerous associated comorbidities has been recognized in HFpEF through increased microvascular dysfunction, nitrosative stress, and insulin resistance (29). Lastly, GO term analysis indicated cellular responses to nitrogen and organonitrogen compounds, processes resulting in changes in secretion, enzyme production, and gene expression as a result of nitrogen compound stimulus. Recently, differences in arterial and coronary sinus metabolomic profiling of patients undergoing cardiac ablation revealed a large net negative nitrogen balance (30), indicative of active proteolysis. Our results provide a potential transcriptional link to account for these metabolite changes, and the aforementioned referenced study provides a small measure of clinical relevance for the model used here.

CARDIOMETABOLIC REMODELING IS AN EARLY SIGNATURE HFpEF DEVELOPMENT.

Because critical mitochondrial ETC components were down-regulated, we hypothesized that derangements in myocardial metabolism likely occur early in the disease process. To evaluate changes in metabolism, we quantified the steady-state abundance of myocardial metabolites in 1-month banded cats versus sham controls. Volcano plot analysis revealed that of the 477 metabolites detected, 82 metabolites were significantly different (FC $\geq$1.25; $P \leq$ 0.1) (**Figure 2A**). Heatmap analysis of the top 50 metabolites and partial least squares-discriminant analysis clustering indicated group-dependent patterning (**Figure 2B,** Supplemental Figure 2A). Visualization of the metabolic networks revealed significant changes in the amino acid superfamily, specifically 1-carbon metabolism (methionine, cysteine, s-adenosylmethionine; subfamily 14), branched chain amino acids (BCAAs; leucine, isoleucine, valine; subfamily 16), and glycine, serine, threonine metabolism (subfamily 19) as pathways highly affected early in HFpEF development (**Figure 2C,** Supplemental Figure 2B). We also observed an increased abundance of BCAAs (eg, isoleucine, valine, leucine) (**Figure 2B**), and pathway enrichment analysis further highlighted amino acids as significantly changed early in HFpEF (**Figure 2D**). Interrogation of the metabolites with the highest variable of importance score revealed glycine and the amino acid gamma-glutamyl-epsilon-lysine as definers of group separation (**Figure 2E**). Interestingly, because glycine constitutes 33% of collagen and gamma-glutamyl-epsilon-lysine is involved in covalently cross-linking extracellular matrix (ECM) proteins in fibrotic tissue (31), this may suggest the activation of fibrotic pathways.

Several lipid species, such as polyunsaturated (subfamily 6), mono- and di-carboxylic fatty acids (subfamily 9), and monoacylglycerols (subfamily 10), were found to be elevated in banded hearts. Acyl-carnitines, used for β-oxidation, did not appear to be changed based on metabolic network visualization (**Figure 2C**). However, *z*-score analysis indicated that some species of acyl-carnitines trended to increase in abundance in banded hearts (Supplemental Figure 3C), suggesting decreased utilization or increased synthesis. The citric acid cycle was also significantly impacted (**Figure 2D**), which, when coupled with our transcriptomics data and the accumulation of acyl-carnitines and BCAAs, is suggestive

FIGURE 6   Skeletal Muscle-omics Profiling Indicates an Energetic Deficit in Early HFpEF Progression
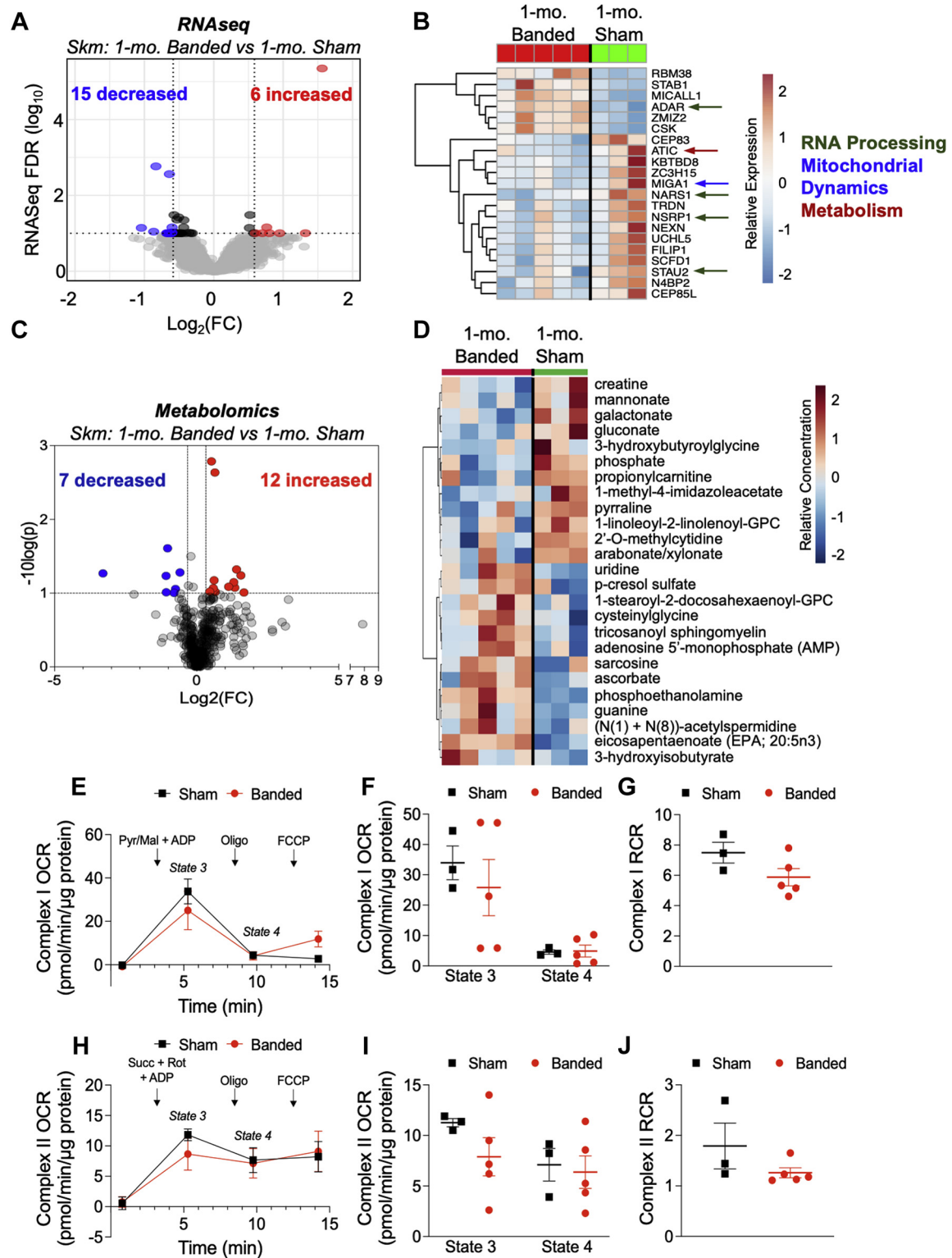
of an overall decrease in oxidative metabolism. Significant enrichment in pathways associated with lipid biosynthesis (eg, cardiolipin, glycerolipid, and phospholipid) (**Figure 2D**) were also observed, indicating changes, not only in catabolism, but also in anabolism. Lastly, nucleotide metabolites associated with purine and pyrimidine metabolism were differentially impacted (**Figure 2C**). Collectively, these results highlight metabolic remodeling of amino acid, lipid, and nucleotide metabolism early in HFpEF-like disease progression, and likely point to an impairment in oxidative metabolism.

METABOLIC REMODELING CORRELATES WITH CARDIAC MITOCHONDRIAL DYSFUNCTION. Mitochondrial dysfunction is a hallmark characteristic of established HFrEF and HFpEF ([32],[33]); however, whether mitochondrial dysfunction precedes or contributes to cardiac dysfunction in HFpEF remains unclear. With our omics analyses suggesting impaired mitochondrial metabolism, we isolated mitochondria from LV tissue biopsies of sham and 1-month banded cats to interrogate state 3 (substrate-mediated), state 4 (oligomycin inhibition of ETC complex V), and maximal respiratory capacity (FCCP-mediated) oxygen consumption rates. Mitochondria from 1-month banded cats demonstrated lower overall respiratory rates, as compared with sham controls (**Figures 3A and 3B**). In the presence of pyruvate + malate (complex I) or succinate + rotenone (complex II), mitochondria from banded cats showed significantly lower state 3 respiration (**Figures 3C and 3D**). Complex I also demonstrated a reduced response to the ETC uncoupler, FCCP, indicating reduced complex I-mediated maximal respiratory capacity (**Figure 3C**). Respiratory control ratios (RCR) were also reduced, suggesting diminished coupling of mitochondrial oxygen consumption to ATP synthesis (**Figure 3E**). To identify potential relationships between metabolite levels and mitochondrial function, we performed a pairwise statistical analysis. Mitochondrial complex I and II state 3 respiratory rates displayed positive correlations with numerous nucleotide phosphates (5'-ADP-ribose; $P = 0.003$; $r = 0.949$; guanosine 5'-triphosphate [GTP]; $P = 0.003$; $r = 0.892$; adenosine 5'-triphosphate [ATP]; $P = 0.012$; $r = 0.823$), suggesting a strong link between mitochondrial

function and myocardial energy state (**Figures 3F and 3H**). Furthermore, complex I maximal respiratory rates (ATP; $P = 0.003$; $r = 0.888$; GTP; $P = 0.016$; $r = 0.805$) and complex II RCR (guanosine 5'-diphosphate [GDP]; $P = 0.007$; $r = 0.848$) positively correlated with these same nucleotide phosphates (**Figures 3G and 3I**). A significant negative correlation between ascorbate and complex II RCR ($P = 0.048$, $r = -0.711$) (**Figure 3I**), which may be indicative of oxidative stress and contribute to diminished coupling of mitochondrial oxygen consumption to ATP synthesis, was also observed. Conversely, numerous monoacylglycerols (eg, 1-dihomo-linolenylglycerol) and diacylglycerols (DAGs; eg, oleoyl-linoleoyl-glycerol) negatively correlated ($P \leq 0.05$) with mitochondrial functional parameters (**Figures 3F, 3G, 3H, and 3I**). Collectively, these results, along with the observed transcriptional down-regulation of ETC-associated components (*MT-ND6*, *ATP5F1B*, and *CHCHD3*), indicate that mitochondrial dysfunction and impairments in energy provision are early features in HFpEF development.

We also observed strong negative correlations with LV lateral free wall fibrosis and the abundances of glutamine ($P = 0.027$; $r = -0.765$), thiamin diphosphate ($P = 0.014$; $r = -0.811$), and metabolites involved in the glutathione cycle (eg, 5-oxoproline; $P = 0.021$; $r = -0.784$; gamma-glutamylglutamate; $P = 0.005$; $r = -0.869$) (**Figure 3J**). Pro-hydroxyproline was also significantly increased in banded hearts (**Figure 2B**). Given that several of these metabolites are in ECM remodeling, it is likely they contribute to initiation of the fibrotic response and resultant tissue fibrosis ([34-39]). The high correlations between the abundance of various metabolites and phenotypic indicators of cardiac remodeling indicate changes in metabolism are not merely consequential, but likely effectors and drivers of disease.

TRANSCRIPTIONAL AND METABOLIC REMODELING DURING HFpEF PROGRESSION INDICATE A SHIFT FROM OXIDATIVE TO GLYCOLYTIC METABOLISM. We examined whether the transcriptional and metabolic changes occurring 1 month post-banding persist following the development of HFpEF characteristics ([16],[17]) and whether this could provide mechanistic

---

FIGURE 6 Continued

Transcriptomic and metabolomic analysis of skeletal muscle (Skm) following 1-month aortic banding compared with sham controls. **(A)** Volcano plot of differentially expressed RNA transcripts indicating the number of genes increased and decreased in expression (FC ≥1.5; FDR ≤0.1); **(B)** heatmap of differentially expressed genes; **(C)** volcano plot analysis showing metabolites with a FC ≥1.25-fold; $P ≤ 0.1$; **(D)** metabolite heatmap profile. n = 3 sham 1-month and 5 banded 1-month. Abbreviations as in **Figures 2 and 3**.

FIGURE 7 Remodeling of Skeletal Muscle 4 Months Post-Banding Is Defined by a Defective Oxidative Metabolism
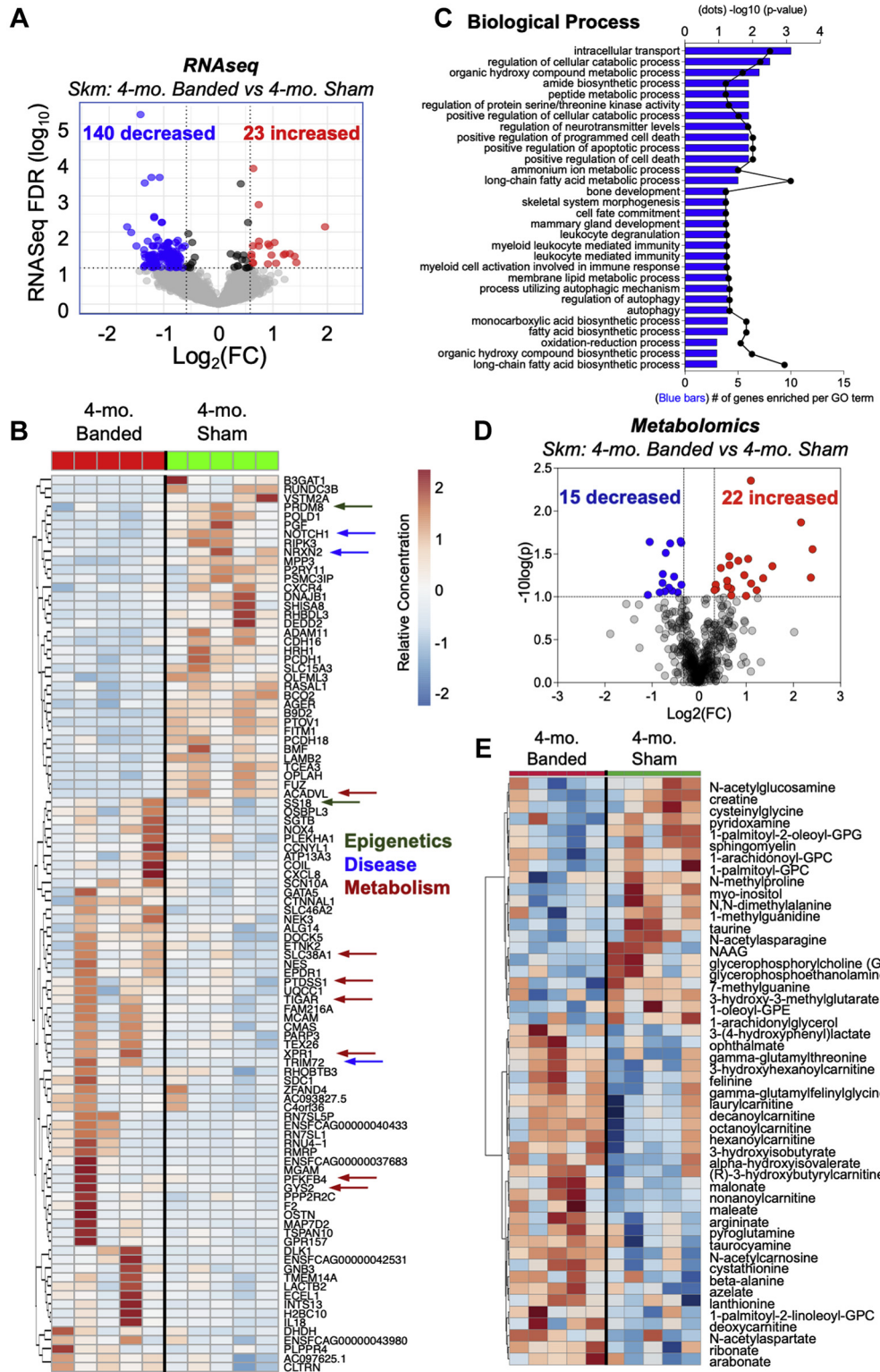
insight to disease progression. Using tissue from a historical cohort previously subjected to 4-month aortic banding (16), RNA-seq identified 59 significantly down-regulated and 109 significantly up-regulated genes (FC ≥1.5 and FDR ≤0.1) (**Figures 4A and 4B**), with GO analysis revealing regulation of metabolic process to have the highest number of associated genes (**Figure 4C**). Down-regulation of *ACADVL*, which catalyzes the first step of β-oxidation, an increase in *PDK1*, which inactivates pyruvate dehydrogenase to reduce pyruvate oxidation, and an increase in *TIGAR*, which influences the activity of PFK, suggest a metabolic preference for aerobic glycolysis over oxidative metabolism (**Figure 4B**). Other metabolic genes altered in expression are related to glycerolipid synthesis (*PTDSS1*), protein glycosylation (*B3GNT7*), and serine metabolism (*VSTM2A*). These transcriptional changes indicate a higher degree of metabolic regulation later in HFpEF, as compared with the 1-month time point where down-regulation of ETC machinery was the only observed metabolic-linked change. In line with this idea, numerous pathways linked to cell signaling (eg, cell surface receptor and GPCR signaling pathways, cyclic-nucleotide-mediated signaling, and negative regulation of signal transduction) were found to be significantly enriched in both biological process and molecular function GO analysis (**Figures 4C and 4D**). Genes associated with cyclic monophosphates (eg, *PDZD3*, *PKIA*, *OSTN*) were differentially expressed, as were *PRKAB2* (AMPK subunit) and *PPP2R2C* (protein phosphatase 2 subunit). AMPK is a primary sensor of the energy state of a cell, and these data suggest that both transcriptional and post-translational modifications (eg, phosphorylation, dephosphorylation, glycosylation) are controlling intermediary metabolism later in disease.

Additional biological processes associated with cellular remodeling (eg, negative regulation of developmental process and cell differentiation) and the immune response (eg, positive regulation of immune system process, neutrophil and granulocyte activation) were significantly enriched in our data set (**Figure 4C**). Additional genes of interest found in our data set were *SCN10A*, a sodium-voltage channel responsible for action potential propagation, and

SYNPO2L, an actin-associated protein linked to heart conduction disease, which were significantly increased in expression (**Figures 4B and 4C**).

Metabolomics at 4 months post-banding revealed a smaller degree of change in fewer metabolites (67 metabolites had a FC ≥1.25; $P \leq 0.1$) as compared with differences 1 month after banding (**Figures 5A, 5B, and 5C**). Citric acid cycle and the Warburg effect were highly enriched due to changes in metabolite abundance (**Figure 6B**). Z-score analyses support the Warburg effect, the favoring of glycolysis over oxidative phosphorylation under aerobic conditions, because glycolytic intermediates were overall reduced, whereas numerous acyl-carnitine species (eg, palmitoylcarnitine) trended to increase in abundance (Supplemental Figures 3A to 3C). We also observed a global decrease in citric acid cycle intermediates (**Figures 5B and 5C**), further indicative of reduced oxidative metabolism. Surprising to us, assessment of mitochondrial function 4 months post-banding revealed a normalization of the mitochondrial dysfunction observed at 1 month (Supplemental Figure 4). Interpreting these results with our transcriptomic data sets suggests metabolic dysfunction in HFpEF progression switches from an initial state of dysfunctional mitochondrial machinery (ie, down-regulation of *MT-ND6*, *ATP5F1B*, and *CHCHD3*) to mitochondrial proteomic compensation and alterations in the transcriptional and post-transcriptional regulation of key metabolic nodes (eg, ACADVL, PDK1, AMPK).

Among the most conserved changes observed over the course of HFpEF progression was the extensive metabolic remodeling of the amino acid superfamily (**Figures 5B, 5C, and 5D,** Supplemental Figure 3C). Unsurprisingly, cardiac fibrosis was more significant 4 months post-banding than at 1 month based on Masson's trichrome staining (16,17). Amino acids critical in ECM remodeling and collagen formation (eg, glutamine, glycine, serine) were decreased in abundance and displayed negative correlations with tissue fibrosis like our findings 1 month post-banding (**Figures 5B, 5C, 5D, and 5E,** Supplemental Figures 3D and 4), suggesting sustained changes in amino acid metabolism underlie the temporal accumulation of interstitial fibrosis during HFpEF progression. BCAAs

FIGURE 7 Continued

Transcriptomic and metabolomic analysis of skeletal muscle (Skm) following 4-month aortic banding compared with sham controls. **(A)** Volcano plot of differentially expressed RNA transcripts indicating the number of genes increased and decreased in expression (FC ≥ 1.5; FDR ≤0.1). **(B)** heatmap of differentially expressed genes (FC ≥1.5; $P \leq 0.1$; total of 163 genes); **(C)** gene ontology (GO) analysis of the biological processes of the differentially expressed genes; **(D)** volcano plot analysis showing metabolites with a FC ≥1.25-fold; $P \leq 0.1$; **(E)** metabolite heatmap profile. n = 5 sham 4-month and 5 banded 4-month. Abbreviations as in **Figures 2 and 3**.

FIGURE 8   Mitochondrial Dysfunction Persists in the Skeletal Muscle During HFpEF Progression
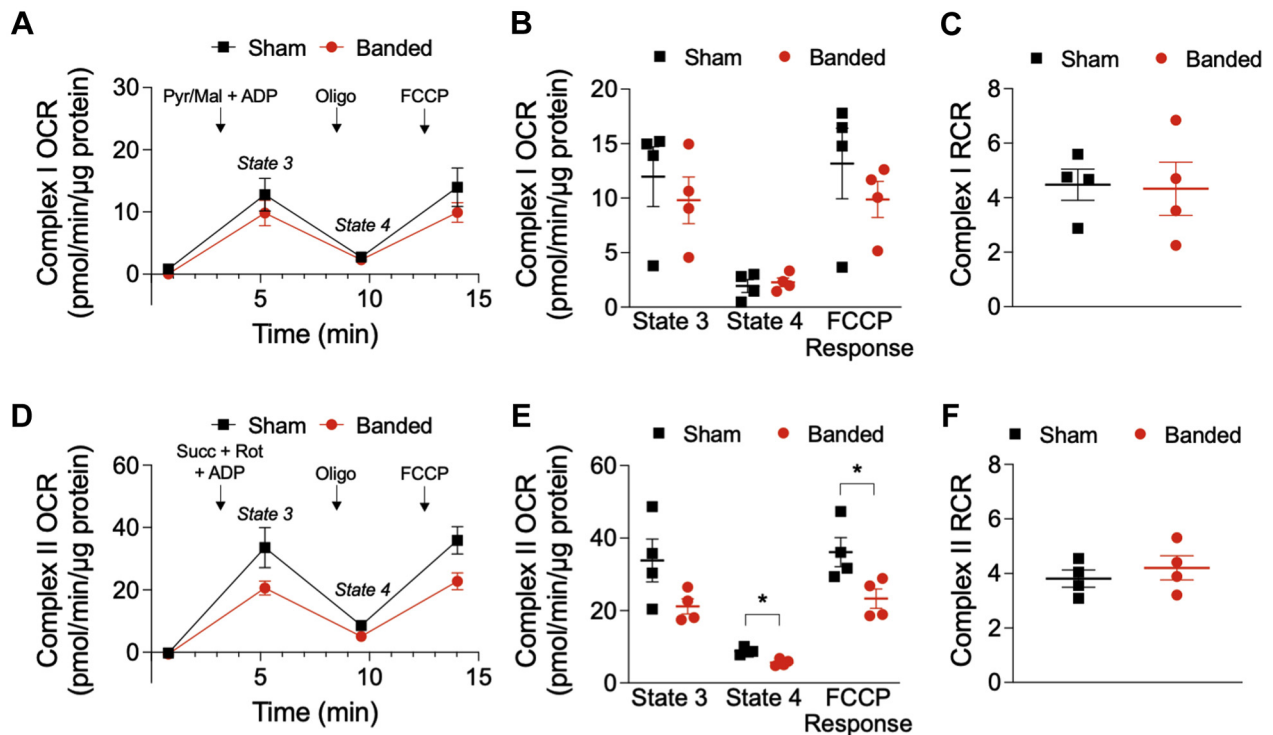
(A and D) Interrogation of mitochondrial function following 4 months of aortic banding: state 3 (substrate-mediated), state 4 (oligomycin inhibition of complex V), and FCCP-mediated (maximal respiratory capacity) oxygen consumption rates in isolated cardiac mitochondria. Quantification of state 3, state 4, and FCCP-mediated rates for **(B)** complex I (pyruvate + malate)-specific substrates and **(E)** complex II (succinate)-specific substrates + rotenone (complex I inhibitor); **(C and F)** Quantification of respiratory control ratios (state 3/state 4), providing an index of oxygen consumption to ATP-production coupling. n = 4 sham 4-month and 4 banded 4-month. Abbreviations as in **Figures 2 and 3**.

were again increased in abundance with high variable of importance scores (**Figures 5B, 5C, 5D, and 5E**, Supplemental Figure 3D). Collectively, the metabolic changes occurring 1 month and 4 months post-banding reveal a conserved signature of amino acid metabolism and a shift in a reliance on aerobic glycolysis as opposed to oxidative metabolism, consistent with the pathological heart ([18,19]).

CARDIOCENTRIC DRIVERS OF SKELETAL MUSCLE REMODELING IN HFpEF PROVIDES INSIGHT INTO POTENTIAL MECHANISMS OF SYSTEMIC DISEASE PROGRESSION. Exertional dyspnea and exercise intolerance are 2 of the major clinical manifestations of HFpEF ([14]). To our knowledge, no studies have investigated whether a primary cardiac insult contributes to peripheral tissue dysfunction and disease progression in an animal model of HFpEF. We isolated skeletal muscle from the same felines banded for 1 month and 4 months to examine skeletal muscle remodeling at the systems level. RNA-seq of

gastrocnemius 1 month post-banding revealed 21 genes differentially expressed (**Figures 6A and 6B**), which were associated with RNA editing and processing (*ADAR*, *NARS1*, *NSRP1*, *STAU2*), de novo purine biosynthesis (*ATIC*), and mitochondrial fusion (*MIGA1*). Metabolically, skeletal muscle was modestly affected as only 19 metabolites were significantly different. However, of those, we noted a reduction in creatine and free phosphate accompanied by an increase in AMP (**Figures 6C and 6D**), suggesting an energetic deficit. An increase in 3-hydroxyisobutyrate, a catabolic intermediate of valine metabolism and a strong marker of systemic and muscle insulin resistance ([40,41]), was also increased in abundance. Assessment of skeletal muscle mitochondrial function revealed reduced complex I and complex II state 3 respiratory rates (**Figures 6E, 6F, 6G, 6H, 6I, and 6J**), suggesting early cardiac remodeling is sufficient to promote peripheral tissue remodeling.

Transcriptomic analysis 4 months post-banding revealed 163 differentially expressed genes, with

numerous metabolic processes, development and cell death/autophagy players identified (**Figures 7A, 7B, 7C**). Of those related to metabolism, several fatty acid-associated genes were highly enriched, with *ACADVL* specifically down-regulated, consistent with the heart. An increase in numerous acyl-carnitine species (**Figures 7D and 7E**) and the expression of regulators of glucose metabolism (*TIGAR*, *PFKFB4*, *GYS2*) (**Figure 7B**) may indicate a fiber-type switch from oxidative to glycolytic, which we have previously reported in this model (17). Consistent with these results, yet unlike our assessment of cardiac mitochondrial function, which was normalized at the 4-month time point, skeletal muscle mitochondrial dysfunction persisted with depressed rates of complex I and complex II respiration (**Figure 8**). We also observed down-regulation of *PRDM8* and up-regulation of *SS18*—genes associated with chromatin and histone modification—as well as *NRXN2*, *TRIM72*, and *NOTCH1*—genes associated with muscular dystrophy—which provide mechanistic insights and potential targets for HFpEF skeletal muscle disease progression.

DISCUSSION

In this study, we used unbiased approaches to define the transcriptional and metabolic changes that occur in a large animal model that recapitulates the cardiopulmonary phenotype of HFpEF. Importantly, this model allowed for the assessment of changes in HFpEF-like disease driven by cardiac dysfunction. Our results reveal distinct changes in cardiac metabolic pathways and transcriptional programs that could shed novel insights into disease progression and provide new therapeutic targets for testing.

METABOLIC RELIANCE FOR ENERGY PROVISION.
Similar to that observed in HFrEF, an early and sustained shift from oxidative to glycolytic metabolism in heart and skeletal muscle during HFpEF progression was observed; however, unlike HFrEF, mitochondrial function was normalized later in disease. At 1 month post-banding, mitochondrial respiratory rates were positively correlated with the abundance of high-energy phosphates (eg, ATP), suggesting an overall energetic deficit. There was also a strong negative correlation with DAGs, the accumulation of which occurs under conditions of reduced beta-oxidation (42). DAG levels are increased in the hearts of HFrEF patients concomitant with a decrease in total fatty acids (43). Interestingly, mice with cardiac-specific deletion of diacylglycerol O-acyltransferase 1, the enzyme converting DAGS to triacylglycerols, display cardiac hypertrophy with preserved systolic function

(44), a metabolic and physiological phenotype similar HFpEF. However, whether this mouse model presents with additional features of HFpEF (eg, diastolic dysfunction, impaired pulmonary mechanics) was not investigated.

Mechanistically, mitochondrial dysfunction is likely a result of reduced expression of key subunits required for complex I (*MT-ND6*), ATP-synthase (*ATP5F1B*), and efficient electron transfer/super-complex formation (*CHCHD3*), indicating deficient metabolic machinery at 1 month. At 4 months, these ETC subunits are no longer down-regulated, and mitochondrial function is normalized, likely suggesting compensation and a later issue with fuel selection or utilization. In support of this hypothesis, the down-regulation of ACADVL and up-regulation of TIGAR and PDK1 implies cardiac metabolism likely becomes more regulated by key rate-limiting steps of metabolism. Post-translational modifications of key metabolic enzymes also likely infer metabolic control at this later time point. For example, protein acetylation of ε-amino groups of lysine residues can greatly affect protein function (45,46). Treatment with a pan-HDAC inhibitor (SAHA) decreased the acetylation of proteins involved in mitochondrial fatty acid oxidation and interestingly enhanced acetylation of enzymes involved in the malate-aspartate shuttle and Krebs cycle (17). Succinate dehydrogenase A hyperacetylation has previously been shown in HF, which results in reduced complex II–driven respiration (47). Collectively, these reports suggest that changes in mitochondrial function and oxidative metabolism are likely driven by post-translational modifications of proteins involved in energy metabolism and the ETC, the regulation of which could be transiently lost during the mitochondrial isolation process and potentially explain why we did not see mitochondrial dysfunction at 4 months. Although previously published studies in animal models and humans at later stages of HFrEF have shown reduced expression of numerous genes and proteins associated with the ETC and cellular metabolism (48-50), our data are more in line with Lai et al (18), who recently reported minimal transcriptional regulation of metabolically linked enzymes 1 month post-aortic banding in mice. Importantly, this progression from deficient machinery to a coordinated substrate preference appears to differ from that of HFrEF, providing a unique feature of HFpEF.

Murine models of HFrEF and human HF patients also display BCAA accumulation because of decreased utilization (51). Decreased oxidation of BCAAs also reduces pyruvate oxidation through the inhibition of pyruvate dehydrogenase via diminished hexosamine

biosynthetic pathway-mediated protein O-GlcNAcy-lation (52), thereby reducing overall oxidative meta-bolism. Our results are supportive of these findings because we observed an increase in BCAA abundance at both early and late stages of disease and a signifi-cant enrichment in glycosylation biological processes in our transcriptomics data. Heart failure also results in the transcriptional down-regulation and inhibitory phosphorylation of the BCAA catabolic enzyme branch-chain alpha-ketoacid dehydrogenase (BCKD) (51), activation of which increases BCAA catabolism preventing adverse cardiac remodeling in models of pressure overload (51) and ischemia /reperfusion (52). Although we did not observe a transcriptional change in BCKD, it is possible that phosphorylation was altered. Whether increasing BCCA catabolism pro-vides similar beneficial effects in HFpEF has yet to be tested and warrants investigation.

In the skeletal muscle, reduced mitochondrial respiration at 1 month was associated with a reduced energy state and the down-regulation of ATIC, an important enzyme for purine synthesis. Skeletal muscle AMP levels were increased, a potential feed-back mechanism to limit purine biosynthesis in the face of a reduced energetic state. Unlike cardiac mitochondria that normalized at 4 months, skeletal muscle mitochondrial function remained depressed and was associated with the down-regulation of *ACADVL* and up-regulation of *PFKFB4* and *TIGAR*, again suggesting a switch from oxidative to glycolytic machinery, such as what is occurring in the heart. What is most interesting here is that the cardiocentric development of HFpEF affects peripheral tissue remodeling providing clues toward the mechanisms underlying progressive exercise intolerance in HFpEF patients.

AMINO ACIDS. Amino acids were among the most conserved and broadly affected changes in our hearts at both early and late HFpEF. Of the many changes, the increase in ascorbate at 1 month likely indicates oxidative stress as high levels of ascorbate can deplete GSH and NADPH, potentially contributing to mitochondrial dysfunction. Furthermore, increased oxidative stress is known to yield DNA strand breaks and adducts resulting in DNA damage. Our tran-scriptomics data revealed a down-regulation of DNA repair genes *RIF1*, *HMBOX1*, and *JMY*, and enrich-ment of biological processes associated with DNA replication, suggesting changes in these important cellular processes.

Cardiac fibrosis is strongly associated with clinical HFpEF (53). Studies in HFpEF myocardial biopsies display significant fibrosis and increased collagen volume fraction (54,55). Remarkably, a positive correlation between myocardial fibrosis and diastolic dysfunction (56) was observed in HFpEF patients, as was myocardial collagen volume with impaired myocardial relaxation (57) and elevated LV diastolic pressures (54,58). Our metabolomics data showed a strong negative correlation between glutamine and LV fibrosis. Recently, comparison of arterial versus coronary sinus blood metabolomics revealed a significantly greater release of glutamine into the coronary sinus in human failing hearts (30). Given the notion that cardiomyocytes use very little glutamine for anaplerosis (59), it is plausible that the observed decrease in glutamine abundance is due to increased fibroblast utilization, which is required for differen-tiation and collagen biosynthesis (34-37). Although we observed a decrease in cardiac glutamine, we believe this is due to differences in consumption versus production rates in the vascular and tissue microenvironment, consistent with other cardiac tis-sue metabolomics studies (19). HFpEF patients also show increased collagen cross-linking and up-regulation of the crosslinker lysyl-oxidase (57); whether our observed increase in the cross-linking metabolite gamma-glutamyl-epsilon-lysine is simi-larly associated is unknown. Although no studies have investigated the role of these cross-linkers in HFrEF, trials using crosslink breakers showed decreased LV stiffness in HFpEF patients; however, no efficacy in HFrEF was noted with the results indicating increased cardiac dilation (60,61).

Although the transcriptional signatures failed to reveal direct biological processes associated with fibrosis, the large inflammatory response at both time points provides a tangible link to tissue fibrosis. Per-ivascular fibrosis is a consequence of systemic and cardiac inflammation by infiltrating immune cells producing profibrotic proteins (eg, TGFβ) (62). Although this type of fibrosis is observed in both HFrEF and HFpEF, it is significantly greater in HFpEF (63). HFpEF patients also have increased serum levels of monocyte chemoattractant protein 1 (MCP1) (64), which is reduced in HFrEF (65), possibly suggesting a distinct inflammatory-mediator of the fibrotic response in HFpEF. In our data set, T-cell activation and differentiation were enriched, and genetic dele-tion or antibody blockade of T-cell expression of the glycoprotein OX40 ligand (OX40L) has been shown to reverse tissue fibrosis (66). Interestingly, glycopro-tein biosynthesis was also enriched 4 months post-banding in our model, which can potentially modulate collagen properties. Although the observa-tion of fibrosis in our HFpEF model was not surpris-ing, unique to our results is the concept that early fibrotic initiation may be causal to HFpEF

development, suggesting therapeutic strategies aimed at targeting the metabolic and transcriptional networks contributing to fibroblast activation and function may improve HFpEF outcomes.

The amino acid 3-hydroxyisobutyrate was found to be elevated at both 1-month and 4-month time points in skeletal muscle and could be important for 2 reasons. First, increased levels of 3-hydroxyisobutyrate are known to reduce insulin sensitivity in oxidative, but not glycolytic, muscle (67). Because HF is associated with skeletal muscle fiber type switching, and our data are suggestive of an increased reliance on glycolytic metabolism, increased 3-hydroxybutyrate likely further exacerbates the energetic deficit indicated by our metabolomics and mitochondrial function results. Second, we observed changes in the expression of *PRDM8* and *SS18*, genes associated with chromatin and histone modification. 3-Hydroxybutyrate has been shown to act as a histone deacetylase inhibitor in muscle (68). This could suggest a metabolic signal to alter, not only histone acetylation, but protein acetylation as well, which we have shown is occurring in HF (17). Targeting of 3-hydroxybutyrate by increasing its oxidation or reducing its synthesis could prove therapeutically beneficial in HFpEF and requires investigation.

NOVEL TARGETS FOR HFpEF. The identification of pathways that distinguish HFpEF from HFrEF are critical for the development of targeted therapeutic strategies; however, the specific mechanisms differentiating these 2 forms of HF are still unknown. Electrocardiography revealed an association between abnormal P waves and HFpEF, but not HFrEF (69). P-wave abnormalities can occur due to atrial hypertrophy and could be indicative of atrial fibrillation. Importantly, the prevalence of atrial fibrillation positively correlates with EF%, but, paradoxically, also with worse cardiovascular outcomes (ie, crude mortality, and hospitalizations remained significant in patients with HFpEF, not HFrEF [70]). Interestingly, we identified *SYNPO2L* and *SCN10A*, genes involved in electrical conduction and associated with atrial fibrillation (71,72), as increased in expression. These genes could provide novel therapeutic targets due to the prevalence of atrial fibrillation in HFpEF.

Understanding the pathophysiology of exercise intolerance, a key clinical feature of HFpEF, is critical for improving patient outcomes. In skeletal muscle biopsies from HFpEF patients, mitochondrial dysfunction was observed and was related to a reduction in oxidative muscle fibers, mitochondrial density, citrate synthase activity, and impaired mitochondrial fusion (73,74). Use of phosphorous

magnetic resonance spectroscopy also revealed rapid depletion of high-energy phosphates during exercise and delayed repletion during recovery, which was significantly worse in HFpEF versus HFrEF patients (75). Our data confirm impaired skeletal muscle bioenergetics because mitochondrial function and high-energy phosphate metabolites were negatively affected, likely a result of fiber-type switching in our model (17). Furthermore, the down-regulation of *MIGA1*, a regulator of mitochondrial fusion, provides potential mechanistic insight into dysfunctional mitochondrial dynamics and changes in the mitochondrial network. Skeletal muscle myopathy also occurs in HF, yet are likely intrinsic to HFpEF and not a secondary consequence or an epiphenomenon (76). Our results revealed altered expression of *NRXN2*, *TRIM72*, and *NOTCH1*, all of which are associated with muscular dystrophy, potentially providing novel targets to address muscle atrophy in HFpEF. Because the current belief is that HFpEF is a systemic disease, our model also suggests the possibility of cardiocentric mechanisms or possibly cardiac-derived circulating factors in mediating skeletal muscle pathogenesis.

STUDY LIMITATIONS. A powerful aspect of systems-based approaches is their utility in providing broad, unbiased insights into disease progression. For example, Gjoneska et al (77) studied a mouse model of Alzheimer disease by integrating omics datasets to profile transcriptional and chromatin dynamics across early to late pathology. Surprisingly, our metabolomic and transcriptomic profiling failed to reveal completely distinct signatures of disease progression in heart or skeletal muscle, which we believe is a limitation of the model system. In the progressive banding model, kittens are banded at 2 months of age, with tissue collection occurring at 1 month and 4 months post-banding. By 6 months of age, the cats have undergone significant growth and development, which obfuscates the ability to resolve differences induced by banding (ie, 2 independent variables leading to the inability to effectively resolve either one). This hypothesis is strengthened by our metabolomic and transcriptomic analyses of 4-month sham versus 1-month sham heart and skeletal muscle, which were found to display greater changes than aortic banding (Supplemental Figures 6 and 7). Although comparing the effects of banding across the 2 time points does yield significantly more changes, it is difficult to tease out which of these are due to disease progression or an artifact of aging (Supplemental Figures 8 and 9), which is why here we compared against age-matched controls. Although this is a limitation of our HFpEF model, our data do indicate distinct metabolic and

transcriptional signatures that are consistent and different at early and late states of disease. Furthermore, recent interventional studies performed in this model have shown improved cardiopulmonary function and outcomes (17), suggesting model validity and translational utility.

An additional limitation of our study is the exclusive utilization of male kittens. We certainly acknowledge the importance of understanding potential sex differences as they relate to the molecular pathways of HF, and our current work in the Houser lab is aimed at investigating potential sex differences in our model.

CONCLUSIONS

In summary, the results presented here demonstrate the power of integrating omics and functional datasets to define complex signatures of cardiac disease states and provide distinct metabolic and transcriptional changes in a model of slow-progressive pressure overload, which closely recapitulates the cardiopulmonary phenotype of HFpEF. Importantly, due to the lack of comorbidities associated with this HFpEF model, the pathological remodeling of skeletal muscle suggests a cardiac-centric contribution to systemic HFpEF progression and pathology. Collectively, these findings reveal novel metabolic and transcriptional features which may allow for the discovery of therapeutic targets to treat and potentially reverse HFpEF-like disease.

FUNDING SUPPORT AND AUTHOR DISCLOSURES

ADDRESS FOR CORRESPONDENCE: Dr John W. Elrod, Center for Translational Medicine, Lewis Katz School of Medicine at Temple University, 3500 N Broad Street, MERB 949, Philadelphia, Pennsylvania 19140, USA. E-mail: elrod@temple.edu.

PERSPECTIVES

COMPETENCY IN MEDICAL KNOWLEDGE: This study used a recently developed feline aortic banding model that recapitulates many of the multifactorial features of HFpEF and shows that mitochondrial and metabolic dysfunction precede the development of the traditional cardiopulmonary features. The systems-based approach employed here identified distinct and conserved changes in amino acids and energy metabolism suggesting metabolic derangements in these pathways as potentially causative in HFpEF disease progression. Transcriptional signatures of early and late HFpEF in our model revealed transcriptional signatures of processes necessary for cellular remodeling. The identification of these metabolic and transcriptional pathways may provide novel therapeutic approaches to prevent and possibly reverse HFpEF disease progression.

TRANSLATIONAL OUTLOOK: Additional preclinical in vivo studies are needed to determine the targetable metabolic and transcriptional pathways that may have therapeutic potential in HFpEF. For example, the promotion of BCAA oxidation in preclinical models of HFrEF has proven beneficial, warranting investigation in models of HFpEF. Identification of numerous genes with potential impacts on arrhythmias, skeletal muscle atrophy, epigenetics, and cellular metabolism could provide targets for therapeutic intervention to treat HFpEF.

REFERENCES

1. National Clinical Guideline Centre (UK). Chronic Heart Failure: National Clinical Guideline for Diagnosis and Management in Primary and Secondary Care: Partial Update [Internet]. London: Royal College of Physicians (UK); 2010 Aug. PMID: 22741186.

2. McMurray JJ, Pfeffer MA. Heart failure. *Lancet.* 2005;365:1877-1889.

3. Kenny HC, Abel ED. Heart failure in type 2 diabetes mellitus. *Circ Res.* 2019;124:121-141.

4. Heidenreich PA, Trogdon JG, Khavjou OA, et al. Forecasting the future of cardiovascular disease in the United States: a policy statement from the American Heart Association. *Circulation.* 2011;123:933-944.

5. Mozaffarian D, Benjamin EJ, Go AS, et al. Heart disease and stroke statistics-2016 update: a report from the American Heart Association. *Circulation.* 2016;133:e38-e360.

6. Ponikowski P, Voors AA, Anker SD, et al. 2016 ESC guidelines for the diagnosis and treatment of acute and chronic heart failure: the Task Force for the diagnosis and treatment of acute and chronic heart failure of the European Society of Cardiology (ESC). *Eur J Heart Fail.* 2016;18:891-975.

7. Reddy YNV, Borlaug BA. Heart failure with preserved ejection fraction. *Curr Probl Cardiol.* 2016;41:145-188.

8. Redfield MM, Chen HH, Borlaug BA, et al. Effect of phosphodiesterase-5 inhibition on exercise capacity and clinical status in heart failure with preserved ejection fraction: a randomized clinical trial. *JAMA.* 2013;309:1268-1277.

9. Yusuf S, Pfeffer MA, Swedberg K, et al. Effects of candesartan in patients with chronic heart failure and preserved left-ventricular ejection fraction: the CHARM-Preserved trial. *Lancet.* 2003;362:777–781.

10. Massie BM, Carson PE, McMurray JJ, et al. Irbesartan in patients with heart failure and preserved ejection fraction. *N Engl J Med.* 2008;359:2456–2467.

11. van Veldhuisen DJ, Cohen-Solal A, Böhm M, et al. Beta-blockade with nebivolol in elderly heart failure patients with impaired and preserved left ventricular ejection fraction: data from SENIORS (Study of Effects of Nebivolol Intervention on Outcomes and Rehospitalization in Seniors With Heart Failure). *J Am Coll Cardiol.* 2009;53:2150–2158.

12. Edelmann F, Wachter R, Schmidt AG, et al. Effect of spironolactone on diastolic function and exercise capacity in patients with heart failure with preserved ejection fraction: the Aldo-DHF randomized controlled trial. *JAMA.* 2013;309:781–791.

13. Cleland JG, Pellicori P, Dierckx R. Clinical trials in patients with heart failure and preserved left ventricular ejection fraction. *Heart Fail Clin.* 2014;10:511–523.

14. Sharma K, Kass DA. Heart failure with preserved ejection fraction: mechanisms, clinical features, and therapies. *Circ Res.* 2014;115:79–96.

15. Conceicao G, Heinonen I, Lourenco AP, Duncker DJ, Falcao-Pires I. Animal models of heart failure with preserved ejection fraction. *Neth Heart J.* 2016;24:275–286.

16. Wallner M, Eaton DM, Berretta RM, et al. A feline HFpEF model with pulmonary hypertension and compromised pulmonary function. *Sci Rep.* 2017;7:16587.

17. Wallner M, Eaton DM, Berretta RM, et al. HDAC inhibition improves cardiopulmonary function in a feline model of diastolic dysfunction. *Sci Transl Med.* 2020;12(525):eaay7205.

18. Lai L, Leone TC, Keller MP, et al. Energy metabolic reprogramming in the hypertrophied and early stage failing heart: a multisystems approach. *Circ Heart Fail.* 2014;7:1022–1031.

19. Sansbury BE, DeMartino AM, Xie Z, et al. Metabolomic analysis of pressure-overloaded and infarcted mouse hearts. *Circ Heart Fail.* 2014;7:634–642.

20. Sweet ME, Cocciolo A, Slavov D, et al. Transcriptome analysis of human heart failure reveals dysregulated cell adhesion in dilated cardiomyopathy and activated immune pathways in ischemic heart failure. *BMC Genomics.* 2018;19:812–812.

21. Riesen SC, Schober KE, Smith DN, Otoni CC, Li X, Bonagura JD. Effects of ivabradine on heart rate and left ventricular function in healthy cats and cats with hypertrophic cardiomyopathy. *Am J Vet Res.* 2012;73:202–212.

22. Hansson K, Haggstrom J, Kvart C, Lord P. Left atrial to aortic root indices using two-dimensional and M-mode echocardiography in cavalier King Charles spaniels with and without left atrial enlargement. *Vet Radiol Ultrasound.* 2002;43:568–575.

23. Russo C, Hahn RT, Jin Z, Homma S, Sacco RL, Di Tullio MR. Comparison of echocardiographic single-plane versus biplane method in the assessment of left atrial volume and validation by real time three-dimensional echocardiography. *J Am Soc Echocardiogr.* 2010;23:954–960.

24. Mattioli AV, Sansoni S, Lucchi GR, Mattioli G. Serial evaluation of left atrial dimension after cardioversion for atrial fibrillation and relation to atrial function. *Am J Cardiol.* 2000;85:832–836.

25. Linney CJ, Dukes-McEwan J, Stephenson HM, Lopez-Alvarez J, Fonfara S. Left atrial size, atrial function and left ventricular diastolic function in cats with hypertrophic cardiomyopathy. *J Small Anim Pract.* 2014;55:198–206.

26. Gibb AA, Epstein PN, Uchida S, et al. Exercise-induced changes in glucose metabolism promote physiological cardiac growth. *Circulation.* 2017;136:2144–2157.

27. Nakada Y, Nhi Nguyen NU, Xiao F, et al. DNA damage response mediates pressure overload-induced cardiomyocyte hypertrophy. *Circulation.* 2019;139:1237–1239.

28. Darshi M, Mendiola VL, Mackey MR, et al. ChChd3, an inner mitochondrial membrane protein, is essential for maintaining crista integrity and mitochondrial function. *J Biol Chem.* 2011;286:2918–2932.

29. Schiattarella GG, Rodolico D, Hill JA. Metabolic inflammation in heart failure with preserved ejection fraction. *Cardiovasc Res.* 2021;117:423–434.

30. Murashige D, Jang C, Neinast M, et al. Comprehensive quantification of fuel use by the failing and nonfailing human heart. *Science.* 2020;370:364–368.

31. El Nahas AM, Abo-Zenah H, Skill NJ, et al. Elevated epsilon-(gamma-glutamyl)lysine in human diabetic nephropathy results from increased expression and cellular release of tissue transglutaminase. *Nephron Clin Pract.* 2004;97:c108–c117.

32. Abel ED, Doenst T. Mitochondrial adaptations to physiological vs. pathological cardiac hypertrophy. *Cardiovasc Res.* 2011;90:234–242.

33. Kumar AA, Kelly DP, Chirinos JA. Mitochondrial dysfunction in heart failure with preserved ejection fraction. *Circulation.* 2019;139:1435–1450.

34. Bernard K, Logsdon NJ, Benavides GA, et al. Glutaminolysis is required for transforming growth factor-beta1-induced myofibroblast differentiation and activation. *J Biol Chem.* 2018;293:1218–1228.

35. Ge J, Cui H, Xie N, et al. Glutaminolysis promotes collagen translation and stability via alpha-ketoglutarate-mediated mTOR activation and proline hydroxylation. *Am J Respir Cell Mol Biol.* 2018;58:378–390.

36. Hamanaka RB, O'Leary EM, Witt LJ, et al. Glutamine metabolism is required for collagen protein synthesis in lung fibroblasts. *Am J Respir Cell Mol Biol.* 2019;61(5):597–606.

37. Lombardi AA, Gibb AA, Arif E, et al. Mitochondrial calcium exchange links metabolism with the epigenome to control cellular differentiation. *Nat Commun.* 2019;10:4509.

38. Asai TT, Oikawa F, Yoshikawa K, Inoue N, Sato K. Food-derived collagen peptides, prolyl-hydroxyproline (Pro-Hyp), and hydroxyprolyl-glycine (Hyp-Gly) enhance growth of primary cultured mouse skin fibroblast using fetal bovine serum free from hydroxyprolyl peptide. *Int J Mol Sci.* 2019;21(1):229.

39. Sato K, Asai TT, Jimi S. Collagen-derived di-peptide, prolylhydroxyproline (Pro-Hyp): a new low molecular weight growth-initiating factor for specific fibroblasts associated with wound healing. *Front Cell Dev Biol.* 2020;8:548975.

40. Jang C, Oh SF, Wada S, et al. A branched-chain amino acid metabolite drives vascular fatty acid transport and causes insulin resistance. *Nat Med.* 2016;22:421–426.

41. Nilsen MS, Jersin RA, Ulvik A, et al. 3-Hydroxyisobutyrate, a strong marker of insulin resistance in type 2 diabetes and obesity that modulates white and brown adipocyte metabolism. *Diabetes.* 2020;69:1903–1916.

42. Timmers S, Nabben M, Bosma M, et al. Augmenting muscle diacylglycerol and triacylglycerol content by blocking fatty acid oxidation does not impede insulin sensitivity. *Proc Natl Acad Sci U S A.* 2012;109:11711–11716.

43. Chokshi A, Drosatos K, Cheema FH, et al. Ventricular assist device implantation corrects myocardial lipotoxicity, reverses insulin resistance, and normalizes cardiac metabolism in patients with advanced heart failure. *Circulation.* 2012;125:2844–2853.

44. Liu L, Trent CM, Fang X, et al. Cardiomyocyte-specific loss of diacylglycerol acyltransferase 1 (DGAT1) reproduces the abnormalities in lipids found in severe heart failure. *J Biol Chem.* 2014;289:29881–29891.

45. McKinsey TA. Isoform-selective HDAC inhibitors: closing in on translational medicine for the heart. *J Mol Cell Cardiol.* 2011;51:491–496.

46. McKinsey TA. Therapeutic potential for HDAC inhibitors in the heart. *Annu Rev Pharmacol Toxicol.* 2012;52:303–319.

47. Horton JL, Martin OJ, Lai L, et al. Mitochondrial protein hyperacetylation in the failing heart. *JCI Insight.* 2016;2(1):e84897. https://doi.org/10.1172/jci.insight.84897

48. Barth AS, Kumordzie A, Frangakis C, Margulies KB, Cappola TP, Tomaselli GF. Reciprocal transcriptional regulation of metabolic and signaling pathways correlates with disease severity in heart failure. *Circ Cardiovasc Genet.* 2011;4:475–483.

49. Bugger H, Schwarzer M, Chen D, et al. Proteomic remodelling of mitochondrial oxidative pathways in pressure overload-induced heart failure. *Cardiovasc Res.* 2010;85:376–384.

50. Gao Z, Xu H, DiSilvestre D, et al. Transcriptomic profiling of the canine tachycardia-induced heart failure model: global comparison to human and murine heart failure. *J Mol Cell Cardiol.* 2006;40:76–86.

51. Sun H, Olson KC, Gao C, et al. Catabolic defect of branched-chain amino acids promotes heart failure. *Circulation.* 2016;133:2038–2049.

52. Li T, Zhang Z, Kolwicz Jr SC, et al. Defective branched-chain amino acid catabolism disrupts glucose metabolism and sensitizes the heart to ischemia-reperfusion injury. *Cell Metab.* 2017;25: 374–385.

53. Schelbert EB, Fridman Y, Wong TC, et al. Temporal relation between myocardial fibrosis and heart failure with preserved ejection fraction: association with baseline disease severity and subsequent outcome. *JAMA Cardiol.* 2017;2:995–1006.

54. Borbely A, van der Velden J, Papp Z, et al. Cardiomyocyte stiffness in diastolic heart failure. *Circulation.* 2005;111:774–781.

55. Mohammed SF, Hussain S, Mirzoyev SA, Edwards WD, Maleszewski JJ, Redfield MM. Coronary microvascular rarefaction and myocardial fibrosis in heart failure with preserved ejection fraction. *Circulation.* 2015;131:550–559.

56. Su MY, Lin LY, Tseng YH, et al. CMR-verified diffuse myocardial fibrosis is associated with diastolic dysfunction in HFpEF. *J Am Coll Cardiol Img.* 2014;7:991–997.

57. Kasner M, Westermann D, Lopez B, et al. Diastolic tissue Doppler indexes correlate with the degree of collagen expression and cross-linking in heart failure and normal ejection fraction. *J Am Coll Cardiol.* 2011;57:977–985.

58. Falcao-Pires I, Hamdani N, Borbely A, et al. Diabetes mellitus worsens diastolic left ventricular dysfunction in aortic stenosis through altered myocardial structure and cardiomyocyte stiffness. *Circulation.* 2011;124:1151–1159.

59. Lauzier B, Vaillant F, Merlen C, et al. Metabolic effects of glutamine on the heart: anaplerosis versus the hexosamine biosynthetic pathway. *J Mol Cell Cardiol.* 2013;55:92–100.

60. Hartog JW, Willemsen S, van Veldhuisen DJ, et al. Effects of alagebrium, an advanced glycation endproduct breaker, on exercise tolerance and cardiac function in patients with chronic heart failure. *Eur J Heart Fail.* 2011;13:899–908.

61. Little WC, Zile MR, Kitzman DW, Hundley WG, O'Brien TX, Degroof RC. The effect of alagebrium chloride (ALT-711), a novel glucose cross-link breaker, in the treatment of elderly patients with diastolic heart failure. *J Card Fail.* 2005;11:191–195.

62. Paulus WJ, Tschope C. A novel paradigm for heart failure with preserved ejection fraction: comorbidities drive myocardial dysfunction and remodeling through coronary microvascular endothelial inflammation. *J Am Coll Cardiol.* 2013;62:263–2671.

63. Dai Z, Aoki T, Fukumoto Y, Shimokawa H. Coronary perivascular fibrosis is associated with impairment of coronary blood flow in patients with non-ischemic heart failure. *J Cardiol.* 2012;60:416–421.

64. Collier P, Watson CJ, Voon V, et al. Can emerging biomarkers of myocardial remodelling identify asymptomatic hypertensive patients at risk for diastolic dysfunction and diastolic heart failure? *Eur J Heart Fail.* 2011;13:1087–1095.

65. Boyle AJ, Yeghiazarians Y, Shih H, et al. Myocardial production and release of MCP-1 and SDF-1 following myocardial infarction: differences between mice and man. *J Transl Med.* 2011;9:150.

66. Elhai M, Avouac J, Hoffmann-Vold AM, et al. OX40L blockade protects against inflammation-driven fibrosis. *Proc Natl Acad Sci U S A.* 2016;113:E3901–E3910.

67. Yamada T, Zhang SJ, Westerblad H, Katz A. {beta}-Hydroxybutyrate inhibits insulin-mediated glucose transport in mouse oxidative muscle. *Am J Physiol Endocrinol Metab.* 2010;299:E364–E373.

68. Sleiman SF, Henry J, Al-Haddad R, et al. Exercise promotes the expression of brain derived neurotrophic factor (BDNF) through the action of the ketone body beta-hydroxybutyrate. *Elife.* 2016;5:e15092. https://doi.org/10.7554/eLife.15092

69. O'Neal WT, Mazur M, Bertoni AG, et al. Electrocardiographic predictors of heart failure with reduced versus preserved ejection fraction: the Multi-Ethnic Study of Atherosclerosis. *J Am Heart Assoc.* 2017;6(6):e006023.

70. Zafrir B, Lund LH, Laroche C, et al. Prognostic implications of atrial fibrillation in heart failure with reduced, mid-range, and preserved ejection fraction: a report from 14 964 patients in the European Society of Cardiology Heart Failure Long-Term Registry. *Eur Heart J.* 2018;39:4277–4284.

71. Tambi R, Abdel Hameid R, Bankapur A, et al. Single cell transcriptomics trajectory and molecular convergence of clinically relevant mutations in Brugada syndrome. *Am J Physiol Heart Circ Physiol.* 2021;320(5):H1935–H1948.

72. van Ouwerkerk AF, Bosada FM, van Duijvenboden K, et al. Identification of atrial fibrillation associated genes and functional noncoding variants. *Nat Commun.* 2019;10:4755.

73. Kitzman DW, Nicklas B, Kraus WE, et al. Skeletal muscle abnormalities and exercise intolerance in older patients with heart failure and preserved ejection fraction. *Am J Physiol Heart Circ Physiol.* 2014;306:H1364–H1370.

74. Molina AJ, Bharadwaj MS, Van Horn C, et al. Skeletal muscle mitochondrial content, oxidative capacity, and Mfn2 expression are reduced in older patients with heart failure and preserved ejection fraction and are related to exercise intolerance. *J Am Coll Cardiol HF.* 2016;4:636–645.

75. Weiss K, Schar M, Panjrath GS, et al. Fatigability, exercise intolerance, and abnormal skeletal muscle energetics in heart failure. *Circ Heart Fail.* 2017;10(7):e004129.

76. Kitzman DW, Haykowsky MJ, Tomczak CR. Making the case for skeletal muscle myopathy and its contribution to exercise intolerance in heart failure with preserved ejection fraction. *Circ Heart Fail.* 2017;10(7):e004281.

77. Gjoneska E, Pfenning AR, Mathys H, et al. Conserved epigenomic signals in mice and humans reveal immune basis of Alzheimer's disease. *Nature.* 2015;518:365–369.

KEY WORDS heart failure, mitochondria, metabolomics, preserved ejection fraction, systems biology, transcriptomics

---

APPENDIX For supplemental figures and tables, please see the online version of this paper.